CZECH TECHNICAL UNIVERSITY IN
PRAGUE

Faculty of Nuclear Sciences and Physical
Engineering

Department of Physics

# Research project

## Production of $J/\psi$ meson in central U+U collisions at the STAR experiment

Jana Fodorová

Supervisor: RNDr. Petr Chaloupka, Ph.D.

Prague, 2015

**Prehlásenie:**


Prehlasujem, že som svoju výskumnú úlohu vypracovala samostatne a použila som len podklady a publikácie uvedené v priloženom zozname.


Nemám závažný dôvod proti použitiu tohto školského diela v zmysle §60 Zákona č.121/2000 Sb., o autorskom práve, o právach súvisiacich s autorským právom a o zmene niektorých zákonov (autorský zákon).


V Prahe dňa ...................

# Acknowledgement

*Title:*

**Production of $J/\psi$ meson in central U+U collisions at the STAR experiment**

*Author:* Jana Fodorová

*Specialization:* Experimental nuclear and particle physics

*Sort of project:* Research project

*Supervisor:* RNDr. Petr Chaloupka, Ph.D.

*Abstract:*

Under normal conditions the basic building blocks of matter (quarks and gluons) are bound within hadrons (e.g. protons, neutrons). The theory of the strong interaction (QCD) predicts that at high temperature and high energy density the hadronic nuclear matter can change into the state of asymptotically free quarks and gluons called quark-gluon plasma (QGP) [1].

It is believed that the Universe was in this state for about few milliseconds after the Big Bang. Our aim is to find out whether the QGP may be created also in the laboratory and what are its properties.

In 2000 the first machine capable to collide heavy ions, the Relativistic Heavy Ion Collider (RHIC), began its operation. Already the data from the first years of the operation indicated the existence of a novel state of hot and dense matter in the evolution of the relativistic heavy-ion collisions [2].

One of the signatures which may refer to the presence of the QGP in the evolution of the collision is the suppression of heavy quarkonium production (i.e. bound states of heavy quark and its antiquark, e.g. $J/\psi$) due to the color screening of the quark-antiquark potential in the QGP. However, there are different other effects which can modify the heavy quarkonium production in heavy ion collisions. To understand these effects we need to study the heavy quarkonium production in different collisional systems.

At the STAR experiment at RHIC, effects of the hot medium on heavy quarkonia have been studied in Au+Au and U+U collisions. Since U nuclei are larger than Au nuclei, it is expected that in the most central U+U collisions the energy density of the created medium is higher than in Au+Au collisions. This makes central U+U collisions a powerful tool for testing of the color screening hypothesis.

In this research project we present current status of our analysis of $J/\psi$ meson production via the di-electron decay channel in 0-5% most central U+U collisions at $\sqrt{s_{\mathrm{NN}}} = 193$ GeV at the STAR experiment. We focus on the extraction of $J/\psi$ signal and its first corrections.

*Key words:* quark-gluon plasma, STAR, RHIC, heavy ion collisions, heavy flavor, heavy quarkonia.

*Názov práce:*
**Produkce $J/\psi$ v centrálních srážkách U+U na experimentu STAR**

*Autor:* Jana Fodorová

*Zameranie:* Experimentálna jadrová a časticová fyzika

*Druh práce:* Výskumná úloha

*Vedúci práce:* RNDr. Petr Chaloupka, Ph.D.

*Abstrakt:*

Za normálnych okolností sú základné stavebné kamene hmoty (kvarky a gluóny) viazané v hadrónoch (napr. v protónoch, neutrónoch). Teória silnej interakcie (QCD) predpovedá, že za podmienok vysokej teploty a hustoty energie môže hadrónová jadrová hmota prejsť do stavu asymptoticky voľných kvarkov a gluónov nazývaného kvarkovo-gluónová plazma (QGP) [1].

Domnievame sa, že vesmír bol v tomto stave niekoľko milisekúnd po Veľkom tresku. Naším cieľom je zistiť, či QGP môže byť vytvorená aj v laboratóriu a aké sú jej vlastnosti.

V roku 2000 bolo spustené prvé zariadenie umožňujúce zrážať tažké ióny, Relativistický urýchľovač ťažkých iónov (RHIC). Už dáta z prvých rokov operácie upozorňovali na možnú existenciu nového stavu horúcej a hustej hmoty vo vývoji relativistických zrážok ťažkých jadier [2].

Jedným z indikátorov prítomnosti QGP vo vývoji zrážky je potlačenie produkcie ťažkých kvarkónií (t.j. viazaných stavov ťažkého kvarku a jeho antikvarku, napr. $J/\psi$) v dôsledku farebného tienenia kvarkovo-antikvarkového potenciálu v kvarkovo-gluónovej plazme. Avšak existujú aj rôzne iné efekty, ktoré môžu ovplyvniť produkciu ťažkých kvarkónií v zrážkach tažkých jadier. Aby sme porozumeli týmto efektom, je potrebné, aby sme študovali produkciu ťažkých kvarkónií v rôznych zrážkových systémoch.

Na experimente STAR na urýchľovači RHIC boli efekty horúceho média na ťažké kvarkóniá študované v zrážkach jadier zlata a uránu. Nakoľko sú jadrá uránu väčšie ako jadrá zlata, očakáva sa, že v najcentrálnejších zrážkach jadier uránu je hustota energie vytvoreného média väčšia ako v zrážkach jadier zlata. Vďaka tomu sú centrálne zrážky uránových jadier silným nástrojom pri skúmaní hypotézy farebného tienenia.

V tejto práci prezentujeme súčasný stav našej analýzy produkcie mezónu $J/\psi$ z rozpadového kanálu $J/\psi \to e^+e^-$ v 0-5% najcentrálnejších zrážkach jadier uránu pri energii $\sqrt{s_{\mathrm{NN}}} = 193$ GeV na experimente STAR. Zameriavame sa na extrakciu signálu $J/\psi$ a jeho prvé korekcie.

*Kľúčové slová:* kvarkovo-gluónová plazma, STAR, RHIC, zrážky ťažkých iónov, ťažké vône, ťažké kvarkóniá.

# Contents

# List of Figures

# List of Tables

# Chapter 1

# Heavy quarkonium production in heavy-ion collisions

In this chapter we explain our motivation for study of $J/\psi$ meson production in central U+U collisions at the STAR experiment. We introduce physical background of our studies including basic information about heavy ion collisions and heavy quarkonium production.

## 1.1 Heavy ion collisions

The Relativistic Heavy Ion Collider (RHIC) [3] has been dedicated to collide beams of heavy ions (e.g. Au+Au, U+U) traveling at nearly the speed of light in opposite directions. There are ca. $10^9$ ions coupled into 111 bunches in each beam which cross at specified intersection points [4]. Despite the large number of ions per bunch, only approximately 2 heavy ion collisions occur per one bunch crossing [5]. Then, still not completely understood collisional evolution begins.

### 1.1.1 Evolution of the heavy ion collisions

The main goal of colliding ultra-relativistic heavy ions is to study the deconfined nuclear medium under equilibrium, the quark-gluon plasma(QGP), which is expected to be one of the phases of the collisional evolution. The medium produced in heavy ion collisions evolves within the proper time range $\tau \sim 10 - 100$ fm/$c$ [6]. The proper time of the system when it enters the QGP phase is estimated to be $\tau_0 \leq 1$ fm/$c$ [6]. Here we briefly describe possible scenario of the heavy ion collision (see also Figure 1.1):

- Immediately after the collision nuclei traverse each other depositing a large amount of energy in the medium in the form of excited virtual quanta. As a result of their deexcitation quarks and glouns are created and interact with each other. In this phase heavy quarks are expected to be produced in interactions of high transferred momenta.

- As the system reaches the thermal equilibrium it can be described by the laws of hydrodynamics. We talk about the quark-gluon plasma phase. The system expands and cools down. When the critical temperature $T_c \simeq 170$ MeV [6] is reached, quarks and gluons can no longer be free within the system and are confined into hadrons. However, it is not clear if the phase transition into the hadron gas happens immediately or if it is proceeded by the mixed phase of quarks, gluons and hadrons.

- The system is in the hadron gas, cools down and expands until chemical freeze-out begins.

- During the chemical freeze-out inelastic scatterings between the hadrons disappear and the particle identities are set. However, hadrons can still interact elastically. Elastic collisions disappear at thermal freeze-out. Finally, particles fly away.

Figure 1.1: Evolution of the heavy ion collision.

## 1.1.2   Centrality of the heavy-ion collisions

Collisions of heavy nuclei can be classified according to different criteria − size and type of colliding nuclei, energy of the collision, etc. For purposes of our analysis it is useful to classify collisions according to the size of the overlapping area of colliding nuclei. As the overlapping zone is larger, there are more nucleons possible to participate in interactions, so the energy density of the medium can be higher. This can turn into higher probability of the QGP formation.

Within this context we talk about the collisional centrality: collisions of heavy nuclei can be central, peripheral or ultra-peripheral depending on the perpendicular distance between the

centers of the nuclei called impact parameter $b$, see Figure 1.2.
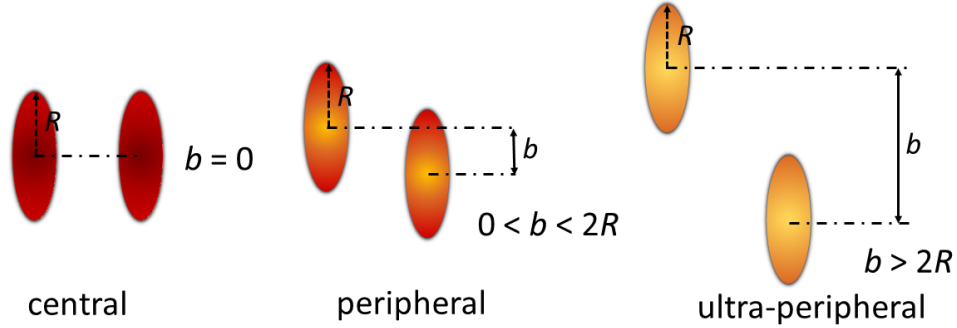


Figure 1.2: Central, peripheral and ultra-peripheral collision.

However, the impact parameter $b$ cannot be measured directly and in collisions of deformed nuclei, in which colliding nuclei can maintain different orientations of different overlapping area at the same $b$, it provides insufficient information about the collisional geometry.

There are two experimental ways which are often used to measure the collisional centrality. The centrality can be determined by measuring the spectators − nucleons which do not participate in interactions. At the STAR experiment, this is provided by the so called Zero Degree Calorimeters (see Chapter 2). One could expect that as the number of spectators decreases the centrality increases. However, not only for the most central but also for the most peripheral collisions the number of spectators is $\sim 0$ since nucleons of the colliding nuclei are not kicked out of the nuclei and, therefore, not measured by ZDCs. Moreover, different orientations of the deformed nuclei at the same value of the impact parameter can turn into different number of measured spectators and, therefore, different centrality values. Therefore, this method of centrality definition is ambiguous. On the other hand, centrality of the collision can be measured by the track multiplicity − more central collisions mean more nucleons participating in the collision which turn to higher multiplicity − more tracks observed in the detector. Figure 1.3 shows the correlation between the charged particle multiplicity $N_{\mathrm{ch}}$ distribution, the number of particles participating in the collision $N_{\mathrm{part}}$ and the impact parameter $b$.

### 1.1.3 U+U collisions

In comparison with spherical Au nuclei, U nuclei are larger and collisions of these deformed "prolate" nuclei provide an opportunity to study the spatial dependence of various properties and effects of the created medium. Within the same system, colliding U nuclei can maintain different spatial orientations and, therefore, allow wider variations of energy density of the created medium.

In case of "tip+tip" configurations where the longest axes of U nuclei are parallel to the beam axis the largest path lengths through the matter and the highest energy densities can be reached. On the other hand, "side+side" configurations where the shortest axes of U nuclei are parallel to the beam provide the shortest paths through the matter. Left panel of the Figure 1.4 illustrates mentioned configurations of colliding U nuclei while the right panel
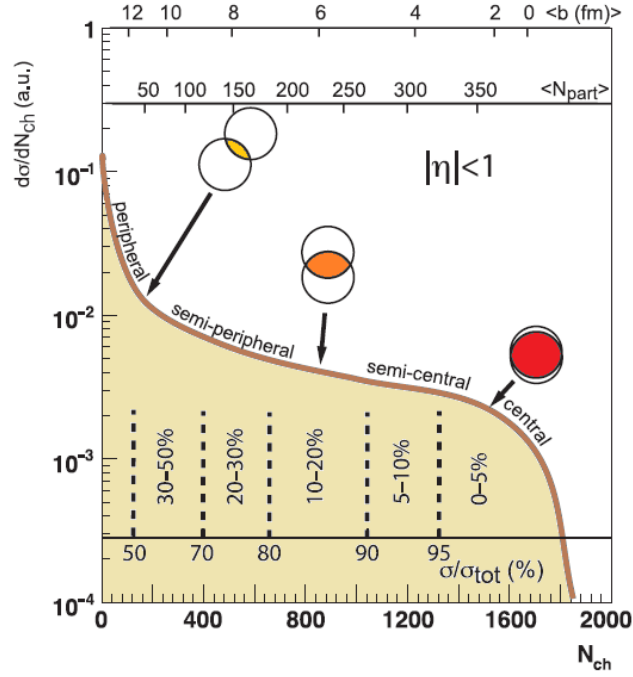
Figure 1.3: Relation between the charged particle multiplicity $N_{ch}$ distribution, the average number of particles participating in the collision $< N_{part} >$ and the impact parameter $b$. Taken from [7].
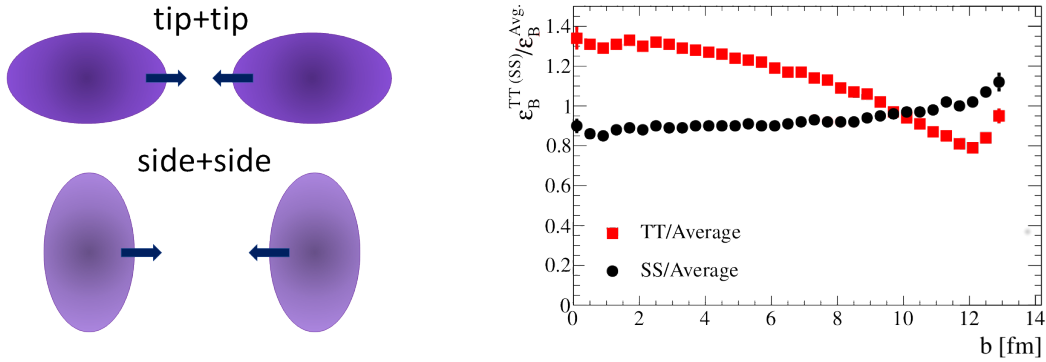


Figure 1.4: Left: Two different configurations of U+U collisions. Right: Comparison of energy densities in "tip+tip" and "side+side" configurations relative to energy density averaged over configurations $\epsilon_B{}^{TT(SS)}/\epsilon_B{}^{Avg.}$ as a function of impact parameter $b$ [8].

shows the comparison of energy densities in "tip+tip" and "side+side" configurations relative to the energy density averaged over configurations as a function of the impact parameter.

4

Compared with Au+Au collisions, the orientation-averaged energy density reached in U+U collisions is expected to be up to 20% higher (in "tip+tip" configurations up to 30%) [8]. This is illustrated in the Figure 1.5 which shows the ratio of estimated energy densities in U+U and Au+Au collisions as a function of centrality. In the most central U+U collisions, the increase of the energy density is the highest − in these collisions the most significant effects of the hot medium are expected to be present. Therefore, detailed study of the most central U+U collisions can provide valuable information about the QGP.
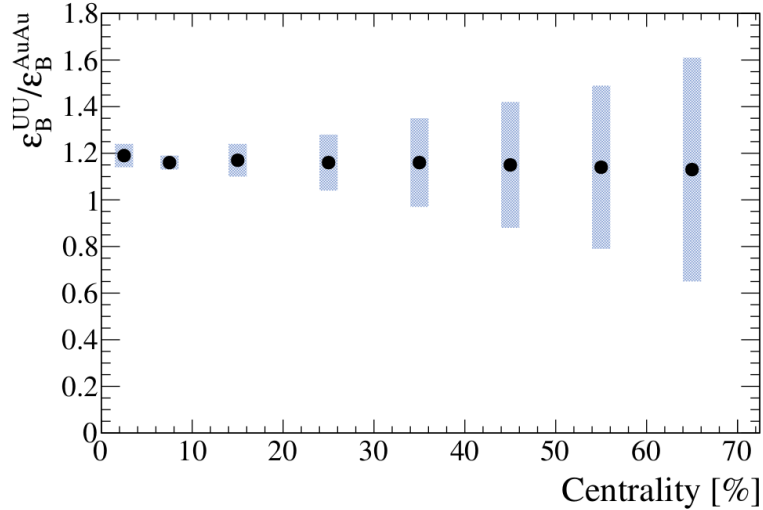


Figure 1.5: Ratio of expected energy density reached in U+U and Au+Au collisions $\epsilon_{\mathrm{B}}{}^{UU}/\epsilon_{\mathrm{B}}{}^{AuAu}$ as a function of centrality [8].

## 1.2   Heavy quarkonia

Heavy quarkonia are bound states of heavy quark $(c, b)$ and its antiquark $(\bar{c}, \bar{b})$. According to whether the quarkonia consist of $c\bar{c}$ or $b\bar{b}$ they are called charmonia (e.g. $J/\psi$, $\chi_c$, $\psi'$) or bottomonia (e.g. $\Upsilon$, $\chi_b$, $\Upsilon'$, $\chi_b'$, $\Upsilon''$). Different quarkonium states differ in mass, binding energy, radius... This can be seen in the Table 1.1 which shows an overview of mentioned quantities.

| State | $J/\psi$ | $\chi_c$ | $\psi'$ | $\Upsilon$ | $\chi_b$ | $\Upsilon'$ | $\chi_b'$ | $\Upsilon''$ |
|---|---|---|---|---|---|---|---|---|
| mass [GeV] | 3.10 | 3.53 | 3.68 | 9.46 | 9.99 | 10.02 | 10.36 | 10.36 |
| $\Delta E$ [GeV] | 0.64 | 0.20 | 0.05 | 1.10 | 0.67 | 0.54 | 0.31 | 0.20 |
| radius [fm] | 0.25 | 0.36 | 0.45 | 0.14 | 0.22 | 0.28 | 0.34 | 0.39 |

Table 1.1: Basic properties of quarkonia − mass, binding energy and radius [9].

### 1.2.1 Heavy quarkonium suppression in heavy ion collisions - melting

Suppression of heavy quarkonium production due to the color screening of the quark-antiquark potential in heavy ion collisions compared with proton-proton collisions has been predicted as a signature of the QGP [10].

If we place quarkonium in the quark-gluon plasma of sufficient temperature $T > T_c$, deconfined quarks and gluons weaken the interaction between heavy quarks, string tension between them vanishes and they can no longer form a bound state.

Potential of the quarkonium in the QGP of the temperature $T$ can be approximately expressed by the formula [11] :

$$V\left(r,T\right) = -\frac{\alpha}{r} exp\left[-r/r_D(T)\right],\tag{1.1}$$

where $r$ is the radius of quarkonium and $r_D$ is the Debye screening radius which sets the distance outside of which the color charge of heavy quark is screened. The Debye screening radius goes down with increasing of the temperature of the medium (approximately as $\sim 1/\sqrt{T}$ [12]). The temperature at which $r_D$ decreases to the quarkonium radius $r$ is the dissociation temperature $T_D$ at which the quarkonium can no longer form a bound state. Since the radii of different quarkonium states vary they are expected to break up at different temperatures. Therefore, measuring the states that survived in the QGP could give us information about the temperature of the medium. Figure 1.6 shows an overview of various model predictions of dissociaton temperatures of different quarkonium states.

### 1.2.2 Other effects on heavy quarkonium production

Suppression of heavy quarkonium production due to the melting is not the only effect which is expected to modify the quarkonium production in heavy ion collisions. Here we briefly describe some other effects which are often considered when talking about modification of heavy quarkonium production.

- **Recombination**

  Suppression of heavy quarkonium production in QGP due to the melting can be compensated by the recombination of single thermalized heavy quarks. At sufficiently high energy the recombination mechanism leads to $J/\psi$ production enhancement. Since the number of charm quarks increases towards more central collisions it is expected that also the number of $J/\psi$ created in process of recombination increases with the centrality [14].

- **Cold-nuclear-matter (CNM) effects**

  In addition to effects on quarkonium production caused by the hot and dense matter there are also CNM effects which can be present also in proton(deuteron)-nucleus collisions in which the QGP phase is not expected to be formed. Therefore, to distinguish between effects of QGP and cold medium, CNM effects need to be studied. Under the term CNM effects nuclear shadowing, Cronin effect and nuclear absorption are often understood.

  - **Nuclear shadowing** denotes modification of nuclear parton distribution functions (nPDFs) relative to PDFs in a proton taking into account the fact that nucleus cannot be simply considered as a superposition of nucleons.
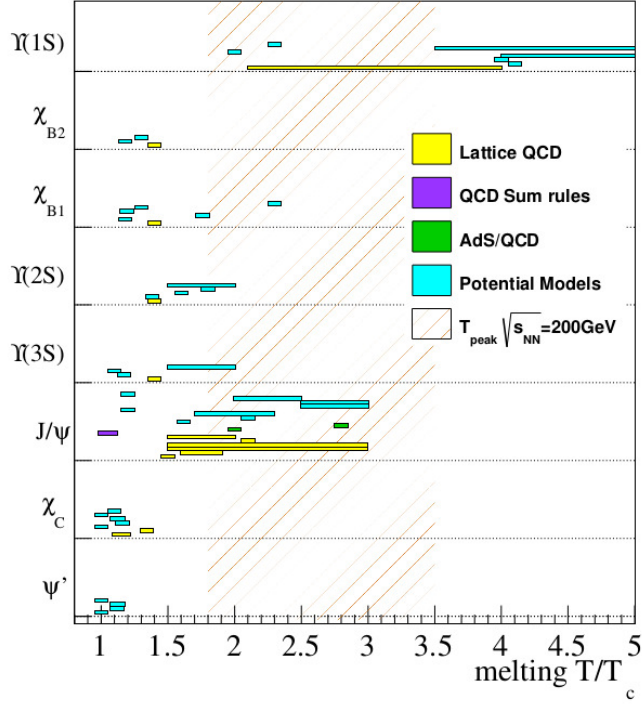
Figure 1.6: The dissociation temperatures of different quarkonium states relative to critical temperature $T/T_c$ − different models calculations (Lattice QCD, QCD sum rules, Ads/QCD, potential models) were used. The shaded band denotes the hydrodynamic estimation for the highest temperature reached in 200 GeV Au+Au collisions. Estimations were performed using different $T_c$ values. Horizontal bars denote the range in which the quarkonium state undergoes modifications until it completely melts [13].

- **Cronin effect** is often interpreted as "transverse momentum kick" [15] which partons (quarks and gluons) acquire in multiple scatterings of partons from the proton off partons from the nucleus in the initial state of the collision resulting in higher $p_T$ of produced quarkonia in p+A (A+A) collisions relative to p+p collisions [16, 17].

- **Nuclear absorption** refers to dissociation of heavy quark-antiquark pairs before they form quarkonium in the initial states of the collision [18]. As these pre-quarkonium states pass by and scatter on nucleons they can be also absorbed by the nucleons with some absorption cross section.

- **Feed-down effects**

  In addition to $J/\psi$ produced directly there are also feed-down $J/\psi$ from higher excited states (in p+p collisions: about 30% from $\chi_c$, 10% from $\psi'$) or from B-mesons decays (in p+p collisions: 10-25 %) [9]. Similarly, in the case of $\Upsilon$ 30% come from $\chi_b(1P)$

states, 10% from direct $\Upsilon'$ states and 10% from $\chi_b(2P)$ states [19]. Since higher excited states are expected to dissociate in QGP easier (at lower temperature) than $J/\psi$ or $\Upsilon$ production of ground states can be suppressed even if the system has not reached their dissociaton temperature.

### 1.2.3  $J/\psi$ measurements in heavy ion collisions at the STAR experiment

To express the modification of e.g. $J/\psi$ production in heavy ion collisions compared with proton-proton collisions we introduce the observable called nuclear modification factor and briefly present results on $J/\psi$ production in Au+Au and U+U collisions at the STAR experiment.

**Nuclear modification factor**

Suppression of heavy quarkonium production in nucleus+nucleus collisions (A+B) compared with proton+proton (p+p) collisions can be quantified by the so called nuclear modification factor $R_{AB}$:

$$R_{AB}(y, p_T) = \frac{1}{<N_{bin}(b)>} \frac{d^2 N_{AB}/\mathrm{d}p_T \mathrm{d}y}{d^2 N_{pp}/\mathrm{d}p_T \mathrm{d}y}.$$ (1.2)

defined as the ratio of number of particles produced in A+B collisions to number of particles produced in p+p collisions scaled to the average number of binary nucleon-nucleon collisions $<N_{bin}>$. Here $R_{AB}$ is given as a function of rapidity $y$ and transverse momentum $p_T$. For collisions of identical nuclei $A = B$.

With no medium effects the yield of heavy quarkonia in heavy ion collisions should scale with the number of elementary binary collisions and resulting $R_{AB}$ should be equal to unity. As it turns out the medium produced in heavy ion collisions can modify this scaling (as shown later) resulting in the effect of suppression $R_{AB} < 1$ or enhancement $R_{AB} > 1$ of the heavy quarkonium production.

**$J/\psi$ in Au+Au collisions**

In the Figure 1.7 we present nuclear modification factor of $J/\psi$ in Au+Au collisions at $\sqrt{s_{NN}} = 200$ GeV at the STAR experiment as a function of number of nucleons participating in collisions $N_{part}$. Results are divided into high and low $p_T$ data and compared to the results of the PHENIX experiment and to model calculations.

Theoretical models (Zhao and Rapp [18], Liu et al. [20]) include $J/\psi$ suppression due to the color screening and enhancement due to the recombination which is expected to be significant in the central collisions and at low $p_T$. Model by Zhao and Rapp also includes contribution from B feed-down and formation time effects on $J/\psi$ production. Except the high $p_T$ prediction of the model by Zhao and Rapp which underestimates the $R_{AA}$ the models describe the data well.

Results show significant suppression at low $p_T$ and towards more central collisions. Suppression can be also seen in the most central high $p_T$ data, which should be not so affected

by the recombination and, therefore, serve as a clearer probe of the color screening, while for the peripheral collisions the suppression vanishes. This observation indicates that the effect of recombination is probably not very significant and supports the idea that the suppression of $J/\psi$ in Au+Au is caused mainly by the color screening.
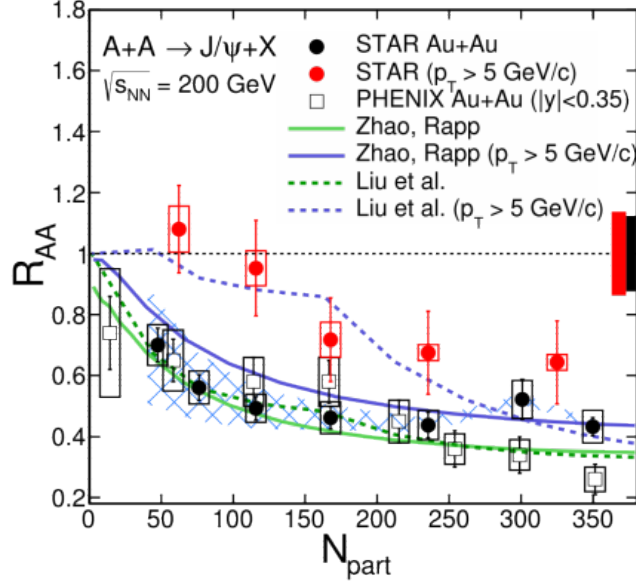


Figure 1.7: $J/\psi$ $R_{AA}$ as a function of $N_{part}$ in Au+Au collisions. High(red circles) and low(black circles) $p_T$ data and compared to PHENIX results (squares) and to model calculations, Zhao and Rapp [18](solid line), Liu et al. [20](dashed line) [21].

## $J/\psi$ in U+U collisions

At the STAR experiment, $J/\psi$ production has been already studied in U+U collisions at $\sqrt{s_{NN}}$ =193 GeV in minimum bias (MB) events and in high-tower triggered (EMC = electromagnetic calorimeter, see Chapter 2) data. Resulting $R_{AA}$ as a function of transverse momentum $p_T$ can be seen in the Figure 1.8. Data are compared with 200 GeV Au+Au collisions. As can be seen from the figure, the suppression of $J/\psi$ production as a function of $p_T$ shows similar trend in both colliding systems.

However, in the most central U+U collisions the highest energy density of the medium is expected to be reached so the effects of the hot medium can be different from that seen in minimum bias collisions and the suppresion seen in the most central U+U collisions can be more significant than in Au+Au collisions. Therefore, it is challenging to look at the centrality dependence of the nuclear modification factor in U+U collisions and compare it with Au+Au collisions. This serves as motivation for our $J/\psi$ studies in 0-5% most central U+U collisions.
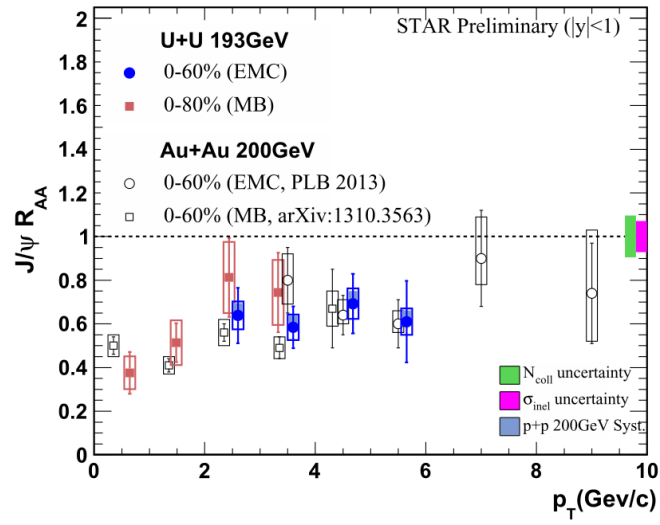
Figure 1.8: $J/\psi$ $R_{AA}$ as a function of $p_T$ in minimum bias (MB) and in high-tower triggered (EMC) U+U and Au+Au collisions [22].

# Chapter 2

# The STAR experiment

The STAR (Solenoidal Tracker at RHIC) detector is an experiment which is dedicated to study strongly interacting matter at high temperatures and high energy densities. Its main objective is detection, tracking and identification of charged particles at midrapidity.

STAR is located at the Relativistic Heavy Ion Collider (RHIC) in Brookhaven National Laboratory in New York, USA. The layout of the RHIC complex can be seen in the Figure 2.1. RHIC is able to collide ions of different masses and at different energies. Moreover, RHIC is the only device in the world capable to collide polarized protons. Until now collisions of p+p, p+Au,p+Al, d+Au, h+Au, Cu+Cu, Cu+Cu, Au+Au and U+U at energies from 62.4 GeV to 500 GeV for protons and from 7.7 GeV to 200 GeV for heavy ions have been performed at RHIC [4].
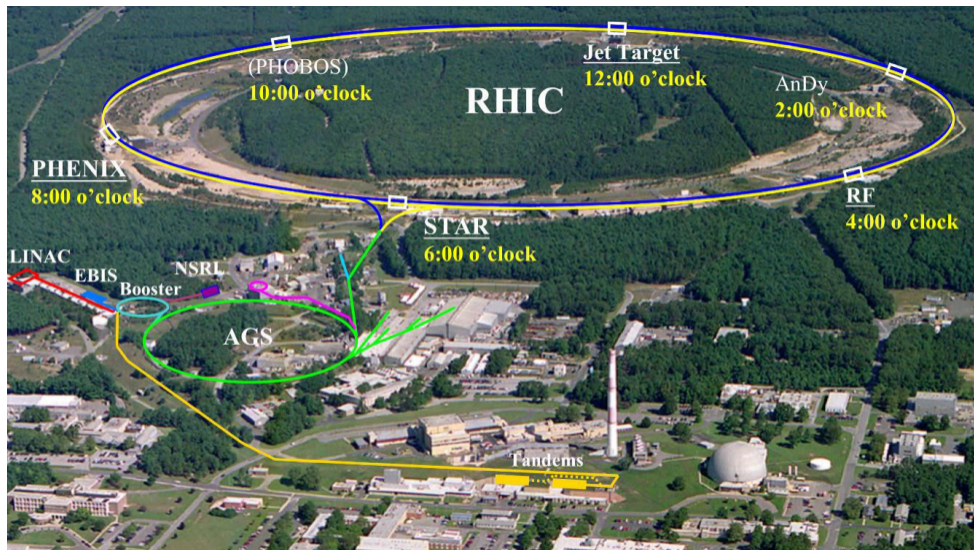


Figure 2.1: The layout of the RHIC complex [23].

RHIC consists of two concentric storage rings which intersect at six points where beams

11

of particles can collide. The massive 1200 tons weighting STAR detector is located at one of these points and shares its axis with the beam-line. It is cylindrical in shape and covers $2\pi$ in azimuth and two units of rapidity around the midrapidity.

STAR consists of various subsystems, schematically shown in the Figure 2.2. These subsystems differ in size, position, material composition, etc. since their function is specific − they can be used for tracking, particle detection or triggering. In following sections detectors important for purposes of our analysis, the Time Projection Chamber (TPC), the Time of Flight (TOF) detector and the Barrel Electromagnetic Calorimeter (BEMC), are briefly presented. Other detectors important for heavy flavor studies are also presented, namely the Heavy Flavor Tracker (HFT) which sits inside the TPC and the Muon Telescope Detector (MTD) located behind the STAR magnet. Since in our analysis we work with centrally triggered data we also introduce the triggering system of the STAR Detector.
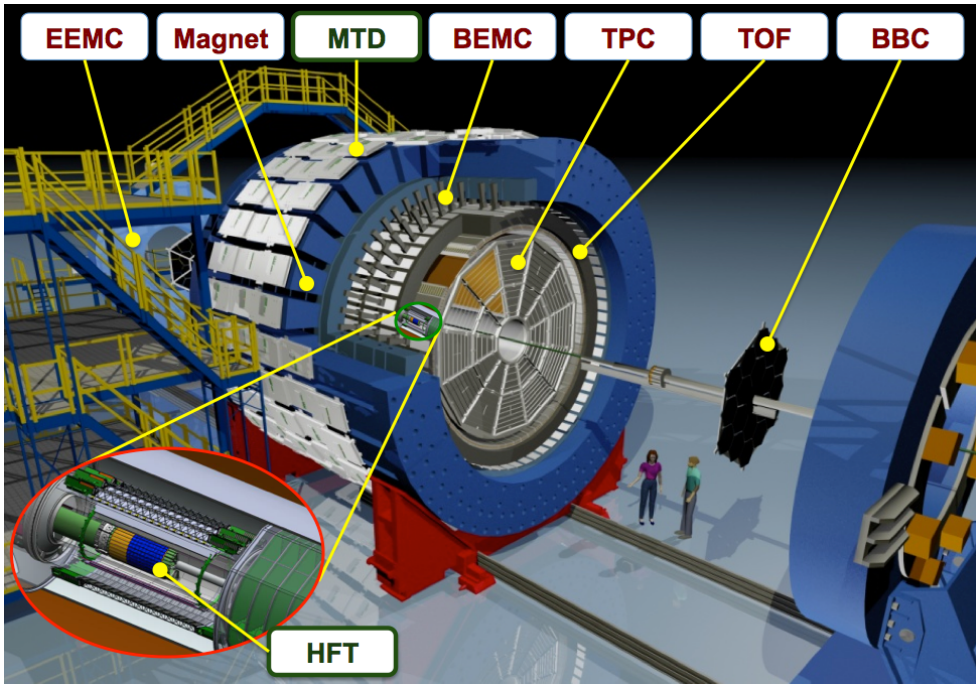


Figure 2.2: The layout of the STAR detector. Picture by Alex Schmah.

## 2.1   Time Projection Chamber

Heart of the STAR detector, the Time Projection Chamber (TPC), is the main tracking device of the STAR detector. It provides identification of charged particles according to their specific ionization energy loss in the material.

The layout of the TPC can be seen in the Figure 2.3. It is cylindrical in shape and surrounds the inner tracking system of the STAR detector located around the beam-pipe. TPC is 4.2 m

long and has an outer diameter of 4 m. It covers pseudorapidity $|\eta| < 1.8$ and full azimuthal angle [24].

TPC sits in a uniform electric and magnetic field. The uniform electric field of ca. 135 V/cm is generated by Central Membrane (cathode membrane) held at the voltage -28 kV and grounded anode end caps while the 0.5 T magnetic field is generated by the solenoidal STAR magnet [24].

TPC is filled with P10 gas (90% Argon, 10% Methane) operating at 2 mbar above the atmospheric pressure.
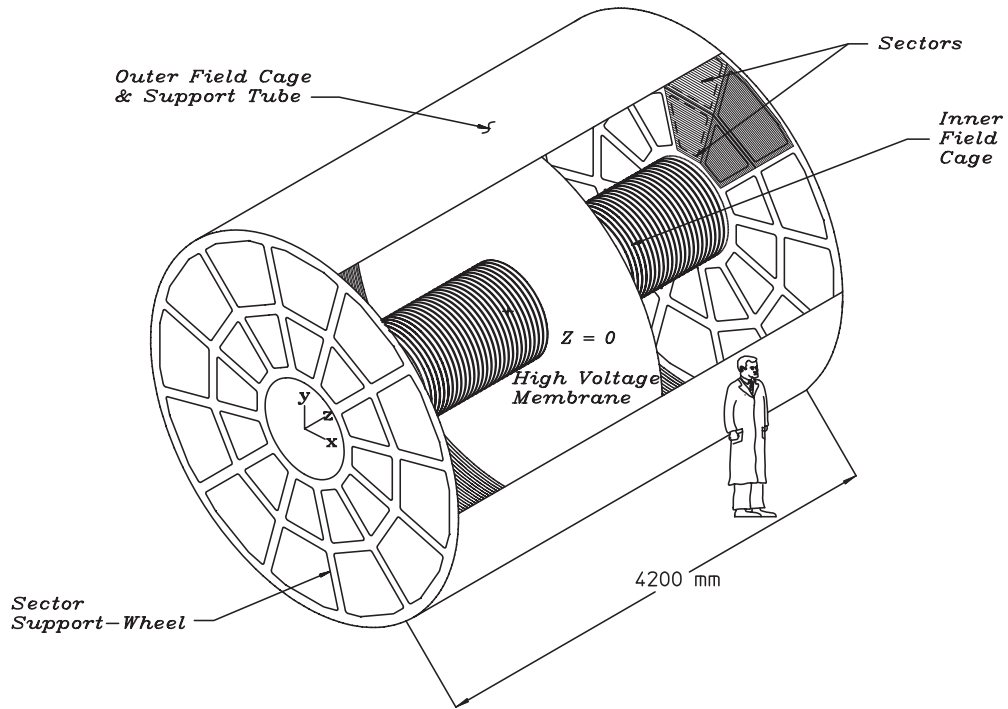


Figure 2.3: The Time Projection Chamber [24].

TPC has anode read out system located on the end caps of the chamber consisting of 136,560 read-out pads based on Multi Wire Proportional Chambers (MWPC) technology. Read-out pads are connected into pad rows and these are divided into 12 sectors. In each sector there are 13 inner and 32 outer pad rows. The inner sectors, located in the area of the highest track density, are equipped with smaller pads than the outer sectors to provide necessary better resolution. Figure 2.4 shows the schematic drawing of one pad plane.

13
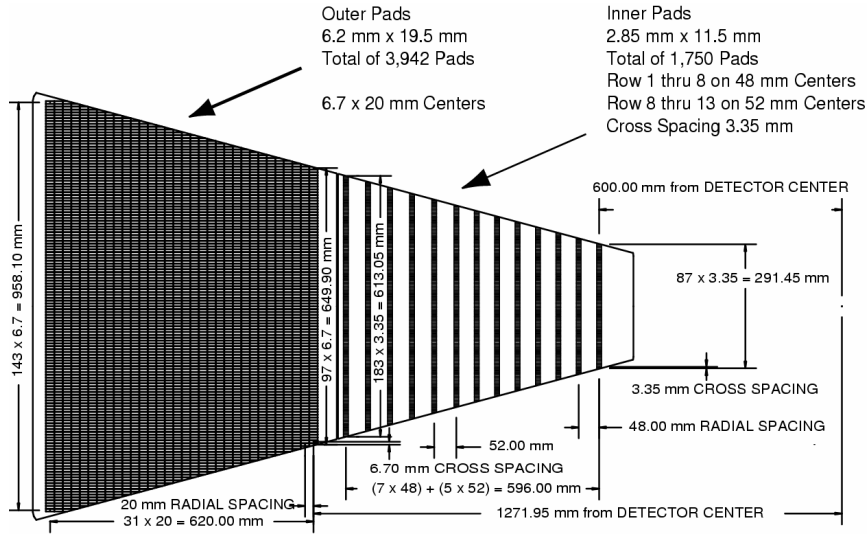
Figure 2.4: The anode pad plane of the read out system of the TPC [24].

### 2.1.1 Particle identification using TPC

As the primary ionizing particle emerging from collision traverses the volume of the TPC it ionizes the atoms of the gas. The electric field of the TPC causes that positive ions travel to the Central Membrane while the (secondary) electrons drift with a constant velocity towards the end caps. Since TPC has anode read-out system the path of the primary particle is reconstructed from the secondary electrons measured on pads on the end caps.

Magnetic field in which the TPC sits curves the trajectories of charged particles. Since the momentum of the particles is proportional to the radius of their curvature, tracking of the particles can determine their momenta. TPC enables to measure momenta over a range of 100 MeV/$c$ to 30 GeV/$c$ [25].

As the primary particles ionize the atoms of the gas they loose the energy which turns out into the charge of secondary electrons collected in the TPC pads. The ionization energy loss of particle per unit of length $dE/dx$ in a given medium (TPC gas) can be calculated for different particle species using the Bichsel functions [26] and compared with measured values.

Figure 2.5 shows the measured and expected energy loss of charged particles in the TPC as a function of the particle momentum. The expected energy loss is calculated via upper mentioned Bichsel functions. As can be seen from the figure, pions, kaons and protons can be well separated in the low $p$ region (for $p < 1$ GeV/$c$). However, towards higher $p_T$ energy loss bands of different particles overlap. In general, using the TPC, particles are identified over a momentum range from 100 MeV/$c$ to greater than 1 GeV/$c$ (we assume 1.4 GeV/$c$). To extend particle identification capabilities towards higher $p_T$ other detectors (e.g. TOF, BEMC) are needed.

14
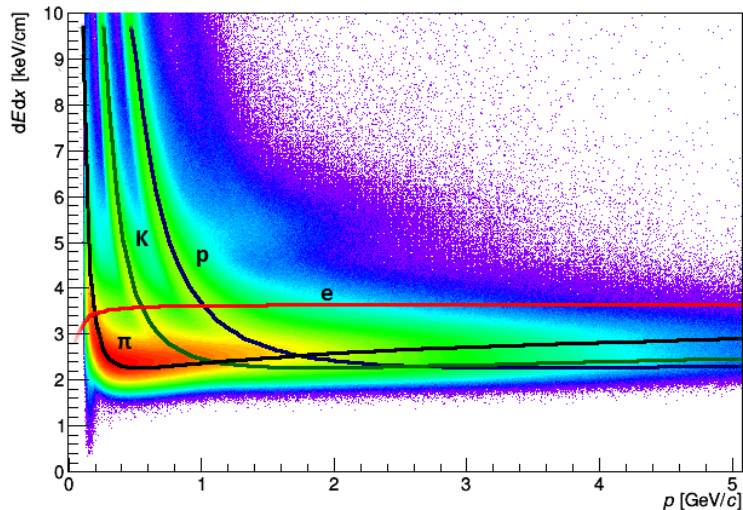
Figure 2.5: The energy loss of charged particles as a function of their momentum in 0-5% most central U+U collisions. Expected values for electrons $e$, pions $\pi$, kaons $K$ and protons $p$ obtained from Bichsel functions [26] are shown as colored curves.

## 2.2 Time of Flight Detector

The Time of Flight (TOF) detector extends the particle identification capabilities of the TPC. Moreover, it is also very important triggering device of the STAR detector (see section 2.4).

TOF creates cylindrical shell of the TPC and covers the pseudorapidity $|\eta| < 0.9$ and full azimuthal angle.

As the name "Time of Flight" indicates, TOF enables to measure the time of flight of the particle. In fact, TOF measures the "stop time" when the signal of the particle in any TOF detection pad is detected. To gain the time of flight we need also the information from STAR Vertex Position Detectors (VPDs) which measure the "start time" of the collision. Then, the time of flight is given as the difference between the stop time and start time. It is often used to express TOF identification capabilities in the words of the average value of the inverse velocity $1/\beta$ given as the ratio of the time of flight and the length $s$ of associated track from the TPC. On the other hand, it can be expressed in the words of mass $m$ and momentum $p$ of the particle as:

$$m = \frac{p}{c}\sqrt{\left(\frac{1}{\beta}\right)^2 - 1}. \tag{2.1}$$

Figure 2.6 shows measured $1/\beta$ as a function of particle momentum for electrons, pions, kaons, protons and deuterons. The expected values are obtained using the particle masses and equation above.

TOF improves particle identification possibilities of TPC. Together with TPC TOF can provide identification of low and intermediate momentum particles − it is effective in separation

15
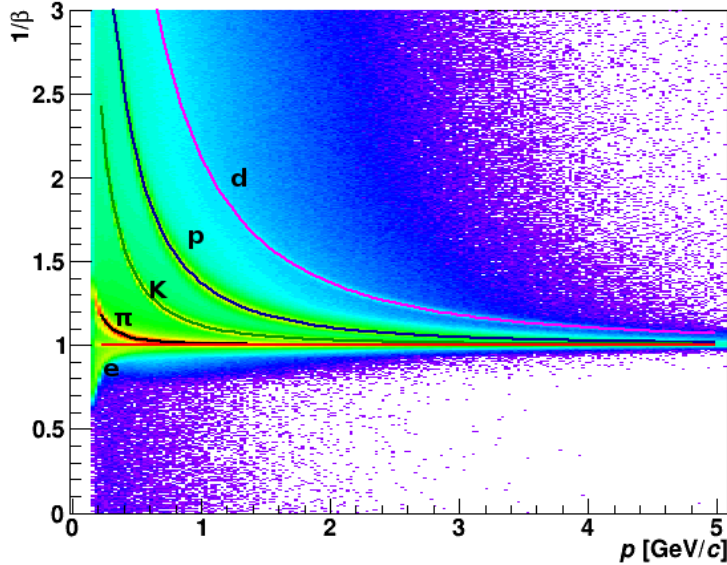
Figure 2.6: $1/\beta$ of charged particles as a function of their momentum in 0-5% most central U+U collisions. Calculated values for electrons $e$, pions $\pi$, kaons $K$, protons $p$ and deuterons $d$ according to 2.1 are shown as colored curves.

of electrons from heavier hadrons at low momenta, pions and (anti)protons are identified for $p <\sim$7-8 GeV/$c$, kaons to $\sim$ 3 GeV/$c$ and electrons from 0.15 GeV/$c$ to 4 GeV/$c$ [27]. To improve the particle identification possibilities towards higher momenta the BEMC is used.

### 2.2.1  Barrel Electromagnetic Calorimeter

The Barrel Electromagnetic Calorimeter (BEMC) measures energy of electromagnetic showers produced by high momentum particles. Hence, it extends particle identification possibilities of STAR towards higher momenta.

BEMC is barrel of diameter ca. 4.4 m. It is located between the TOF detector and the STAR magnet. It covers pseudorapidity $|\eta| < 1$ and full azimuthal angle $\phi$. It consists of 120 calorimeter modules of the size $\Delta\eta \times \Delta\phi \simeq 1 \times 0.1$, each of each of which is segmented into 40 towers, 2 in $\phi$ and 20 in $\eta$, with each tower being 0.05 in $\Delta\phi$ by 0.05 in $\Delta\eta$. The schematic drawing of the BEMC module is illustrated in the Figure 2.7. Each module consists of a lead-scintillator stack and Barrel Shower Maximum Detectors (BSMD)[28]. As high energy particles pass the layers of lead and scintillator they produce electromagnetic showers. Lead plates are absorbers, they convert the energy of "original particles" into multiple ones with smaller energy, while the role of the scintillator layers is to convert the energy of particles from shower to energy of photons and to sample this energy.

Since BEMC has a total radiation length $20X_0$ [28] electrons are expected to deposit their whole energy in the calorimeter while hadrons not. Therefore, for high momentum electrons energy-to-momentum ratio $E/pc$ (where $E$ is energy deposited in the BEMC towers) is $\sim 1$

while for hadrons it is less than 1. So, at high momentum the BEMC towers provide electron-hadron separation via $E/pc$.

The role of the BSMD is to provide spatial resolution of the position and the shape of the shower. Therefore, they are located at the depth of 5 radiation lengths where the electromagnetic showers are expected to be fully developed.
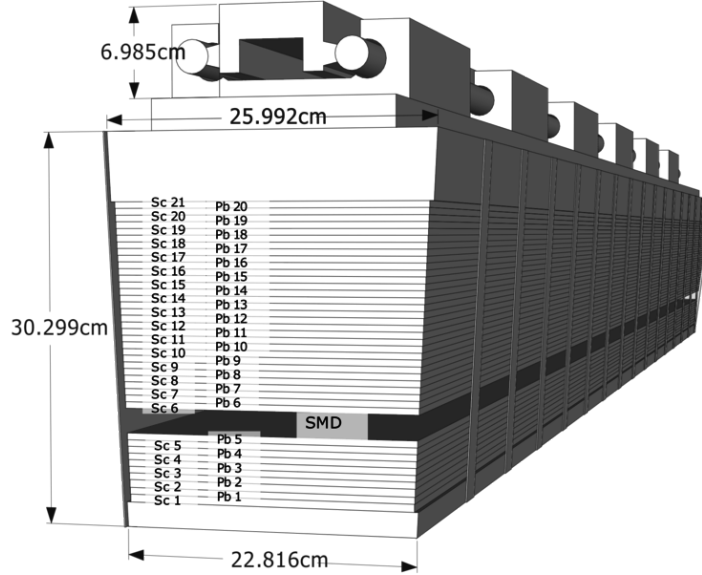


Figure 2.7: Schematic drawing of the BEMC module [29].

## 2.3  Heavy Flavor Tracker

HFT is located around the beam-pipe in the central part of the STAR detector. It consists of different subsystems: two layers of the silicon pixel detector (PIXEL) which surround the beam pipe at the distance of 2.5 cm and 7 cm respectively and the intermediate silicon tracker (IST) which consists of two barrel layers with radii of 12 cm (IST1) and 17 cm (IST2)[30].

Sketch of the location of the Heavy Flavor Tracker subsystems and its photograph can be seen in the Figure 2.8.

Inner tracking system of the STAR detector includes also the Silicon Strip Detector (SSD) located between the HFT and TPC at the distance of 23 cm. It measures the 2D position of hits and energy loss of charged particles.

Main physical motivation for the Heavy Flavor Tracker (HFT) is to improve and extend capabilities of heavy flavor production measurements at STAR by the measurement of displaced vertices and to provide the direct topological identification of open charm hadrons [30]. Another advantage of HFT is the the ability to distinguish between charm and bottom contributions. Precise measurements of open heavy flavor yields with the help of the HFT enable to extrapolate

17

to the total charm quark production yield and this is important in studies of charmonium production and suppression.
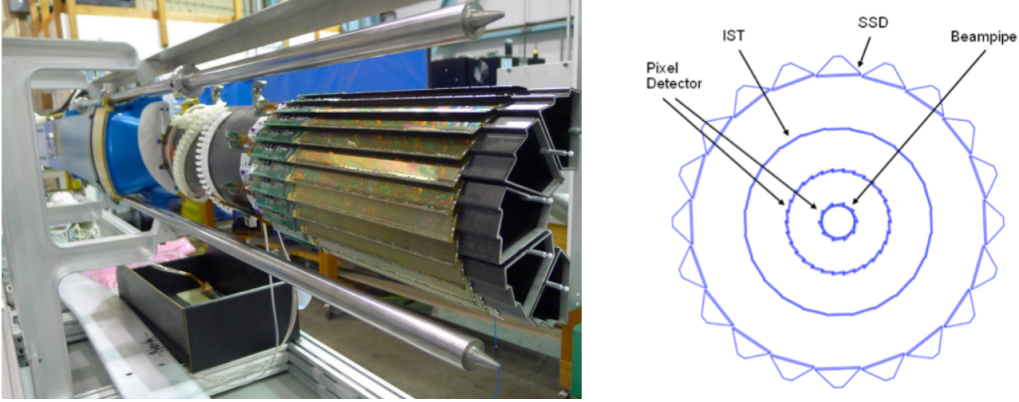


Figure 2.8: The Heavy Flavor Tracker. Left: The photograph of the HFT [31]. Right: Sketch of the subsystems of the HFT [31].

### 2.3.1 Muon Telescope Detector

Muon Telescope Detector (MTD) is located behind the STAR magnet in the distance of ca. 400 cm from the beam pipe (see Figure 2.2). The STAR magnet, used as an hadron absorber, provides background shielding. Sketch of the MTD detector can be seen in the Figure 2.9. MTD covers 45% of the azimuth angle and the pseudorapidity $|\eta| < 0.5$.
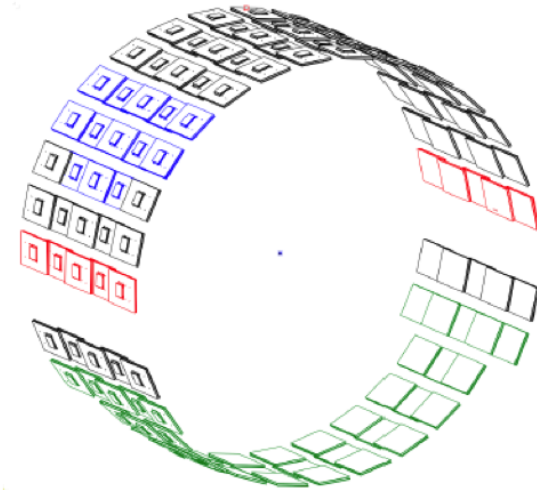


Figure 2.9: The schematic drawing of the Muon Telescope Detector [32].

MTD modules, basic detection blocks of MTD, are based on Multi-gap Resistive Plate

Chambers (MRPC) technology which is similar to technology used in TOF. "Body" of the MRPC module consists of 6 resistive glass plates resulting in a total of 5 gas gaps. Gas gaps are filled with a mixture of 95% Freon and 5% Isobutane [33]. Charged particles traversing the volume of the MTD modules ionize molecules of the gas and create electron avalanches which are then detected on the anode strips. The role of the resistive glass plates is to absorb some electrons from avalanche to improve spatial resolution of the modules.

The Muon Telescope Detector (MTD) is important due to its capability to identify muons which do not participate in strong interactions and, therefore, are interesting probes of the strongly-interacting quark-gluon plasma. MTD enables detection of di-muon pairs from QGP thermal radiation, quarkonia decays or light vector meson decays. It also allows open heavy flavor measurements using semileptonic decays and electron-muon correlations. Although some of these topics can be studied through electrons or photons, they have larger backgrounds than muons. Another advantage of muons is that unlike the electrons, they are not so affected by Bremsstrahlung radiation, i.e. they do not loose so much energy, and thus can provide better mass resolution of vector mesons and quarkonia, especially different $\Upsilon$ states [34].

Figure 2.10 shows $J/\psi$ signal in p+p collisions at $\sqrt{s_{\mathrm{NN}}} = 500$ GeV. reconstructed via the decay channel $J/\psi \to \mu^-\mu^+$ using MTD.
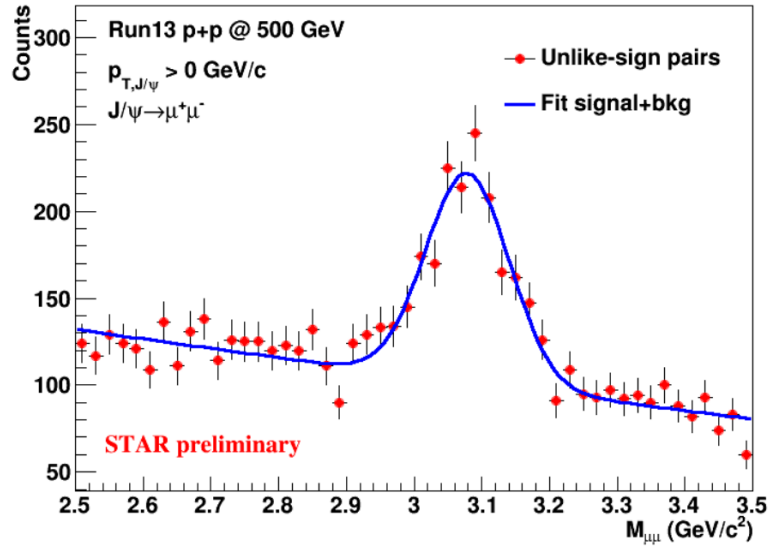


Figure 2.10: $J/\psi$ signal reconstructed using MTD [35].

## 2.4   Triggering System

Triggering system of the STAR detector detects collisions, makes decisions which events should be recorded and whether to "switch on" slow detectors (e.g. TPC) required primarily for tracking and particle identification. STAR triggering system consists of four levels of logic labeled L0, L1, L2 and L3. The high level trigger L3 provides the information from the slow

19

detectors [36] while L0, L1 and L2 are based on the information from the fast detectors − L0 trigger must make decisions in < 1 microsecond based on total event multiplicity, variations in multiplicity topology, event vertex location and remnant nucleon multiplicities [37], L1 and L2 make decisions based on event by event fluctuations in charged particle and energy distributions [36]. Below we present some important functions of fast detectors of the STAR triggering system.

- The two **Vertex Position Detectors** (VPDs) are located very close to the beam pipe ca. 5.6 m from the intersection point. They detect fragments from the collisions which do not participate in interactions. The time difference between the signals of the East and the West VPD determines the primary vertex position of the collision, the time average determines the start time of the collision needed for TOF [38]. VPDs are used as a primary minimum bias trigger and also central trigger.

- The two **Beam Beam Counters** (BBCs) are located ca. 3.5 m from the intersection point of the STAR detector. They consist of two layers of hexagonal blocks which surround the beam pipe. BBCs can determine the collisional vertex position and centrality, however primarily they are are used to monitor beam conditions [39].

- The two **Zero Degree Calorimeters** (ZDCs) are situated at 18.25 m from the intersection point outside of the RHIC magnets. Detecting the Čerenkov radiation the ZDCs measure the number of spectator neutrons from collisions. They are used for triggering on central collisions and for beam monitoring [40].

- The **Time Of Flight** (TOF) detector is used to trigger on central collisions by requiring a high occupancy of hits.

- The **Barrel Electromagnetic Calorimeter** (BEMC) triggers on events with a large deposit of energy in BEMC tower or tower cluster, corresponding to the production of a jet or high $p_{\mathrm{T}}$ particle [39].

- The **Muon Telescope Detector** (MTD) triggers on events with $\mu-\mu$ requiring at least two hits on MTD, in coincidence with TOF it triggers on cosmic rays and in coincidence with VPDs and BEMC towers it triggers on minimum bias and $e-\mu$ events [41].

# Chapter 3

# Analysis of $J/\psi$ in 0-5% most central U+U collisions − signal extraction

In this chapter we present current status of our analysis of $J/\psi$ production in 0-5% most central U+U collisions at the STAR experiment.

$J/\psi$ raw yield was reconstructed via the di-electron decay channel $J/\psi \to e^+e^-$ with branching ratio ~5.9%. The method of $J/\psi$ signal extraction we used is described as a sequence of different criteria which events, tracks and $J/\psi$ decay electron candidates had to satisfy.

## 3.1   Data, triggers and event selection

In our analysis we used the data taken from U+U collisions which were recorded at RHIC at the center-of-mass energy $\sqrt{s_{NN}} = 193$ GeV in Run 12 in 2012. For the purposes of study central collisions we used events which satisfied the 0-5% centrality triggers, namely those labeled central-5 and central-5-protected. These triggers require the TOF multiplicity, i.e. the number of hits in TOF, and the ZDC coincidence rate to be above some certain values. Moreover, there are also some additional requirements on ZDC signal and also BBC signal which differ from run to run.

Attribute "protected" denotes that events satisfying corresponding trigger are already corrected on pile-up events. Pile-ups originate from following process: there is higher frequency of collisions than TPC read-out frequency − tracks from multiple events can be read out at the same time and then multiple vertices of single collision reconstructed. Here is an overview of applied triggers and corresponding trigger IDs according to STAR notation:

- central-5 : 400101, 400111, 400121,

- central-5-protected : 400102, 400122, 400132, 400142.

In our analysis ca. 115 M of 0-5% most central events satisfying the "trigger cut" were used. Figure 3.1 shows the multiplicity distribution of events used in our analysis. However,

since the 0-5% centrality triggers have low thresholds on events to be classified as central, there can be significant amount of events which, in fact, do not belong to this centrality class. As a result, our multiplicity distributions need to be corrected. We plan to perform these corrections in the nearest future.
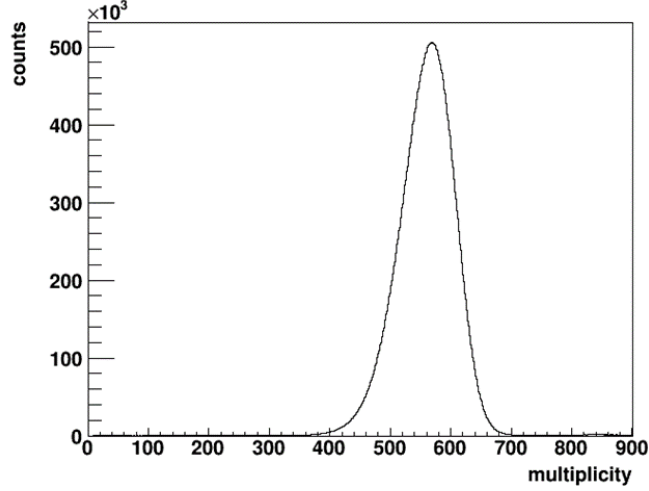


Figure 3.1: Multiplicity distribution of 0-5% most central events according to TOF+ZDC.

For further analysis we selected only those events for which the longitudinal distance (i.e. in the direction of the $z$-axis) between their primary vertex (a place where the collision happens) and the center of the detector ($v_Z$) was lower than 30 cm (see left panel of the Figure 3.2). This
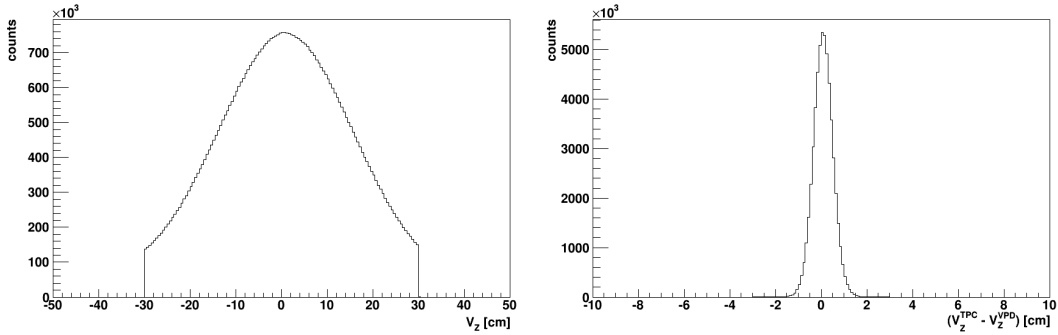


Figure 3.2: Event cuts shown on our data sample. Left: Applied condition on the $z$-coordinate of the primary vertex position. Right:Applied condition on the difference between the $z$-coordinate of the primary vertex given by TPC and VPDs.

requirement was used since we wanted to analyze only collisions in the center of the detector. The $z$-coordinate of the primary vertex is determined by TPC as the intersection point of the tracks of reconstructed particles ($v_Z^{\mathrm{TPC}}$) but it can be determined also by the VPDs ($v_Z^{\mathrm{VPD}}$). To remove the pile-up events we analyzed only those events for which $|v_Z^{\mathrm{TPC}} - v_Z^{\mathrm{VPD}}| < 3$ cm

(see right panel of the Figure 3.2). Applying the event cuts we reduced the number of analyzed events to $\sim$ 56 M.

## 3.2   Trajectory cuts

From events satisfying event cuts we selected only good-quality particle trajectories which we used in further analysis. Primary tracks had to fulfill following criteria :

- The distance of the closest approach (DCA) of the track to the primary vertex had to be less than 3 cm.

- Particle trajectories are reconstructed by fitting the hits on the TPC pads. To ensure good quality of reconstructed tracks the minimal number of reconstructed hits in TPC was required to be 20.

- The ratio of fitted hits to possible hits (maximum number of hit points) on the TPC pads had to be larger than 0.51. This requirement was used to remove split tracks which decrease mentioned ratio.

- Only tracks with pseudorapidity $\eta < 1.0$ were accepted.

Four panels of the Figure 3.3 show application of different cuts on the particle trajectories.
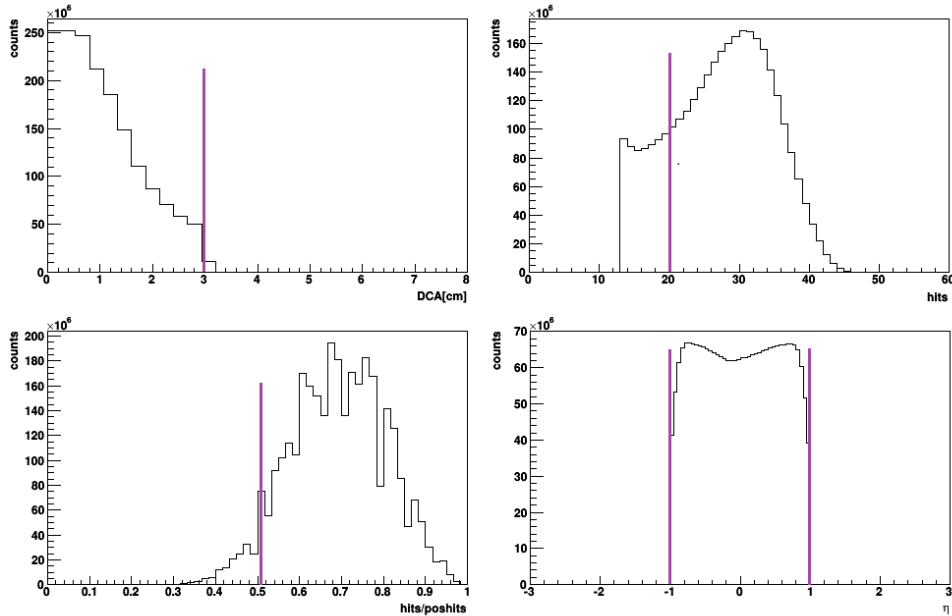


Figure 3.3: Illustration of different cuts applied on primary trajectories.

We also applied cut on transverse momenta of reconstructed tracks to be above given value. We used different threshold values: $p_T > 0.2$, 0.8, 0.9, 1.0, 1.2, 1.4 GeV/$c$ and observed how

23

this $p_T$ cut affected the $J/\psi$ signal. This criterion is discussed in more detail in the last section of this chapter.

## 3.3   Cuts on electron candidates

From the tracks satisfying criteria described in previous section we selected those which could represent electrons. Our electron candidates had to fulfill cuts on TPC, TOF and BEMC signal described below.

### 3.3.1   TPC cut

As already mentioned, TPC provides identification of charged particles according to their specific energy loss $dE/dx$ in the TPC gas. Figure 2.5 shows measured energy loss of different particle species and their expected energy loss given by Bichsel functions [26]. Our aim was to analyze electrons. Therefore, one could expect that good way how to find the electrons is to take only those tracks for which the $dE/dx$ fluctuates around the theoretical value $dE/dx_{\mathrm{Bichsel}}$ for electrons. This is connected with the variable $n\sigma_{\mathrm{e}}$ which gives $dE/dx$ normalized to $dE/dx_{\mathrm{Bichsel}}$ in the logarithm and scaled by the $dE/dx$ resolution $\sigma_{dE/dx}$:

$$n\sigma_{\mathrm{e}} = ln\left(\frac{dE/dx}{dE/dx_{\mathrm{Bichsel}}}\right)/\sigma_{dE/dx} \tag{3.1}$$

We required $n\sigma_{\mathrm{e}}$ to be in the range between $-1.5$ and $2.0$. The asymmetric cut is used to decrease the contamination from pions for negative $n\sigma_{\mathrm{e}}$, see Figure 3.4 for electron candidates with $p_T > 0.2$ GeV/$c$. TPC cut was required for all electron candidates.
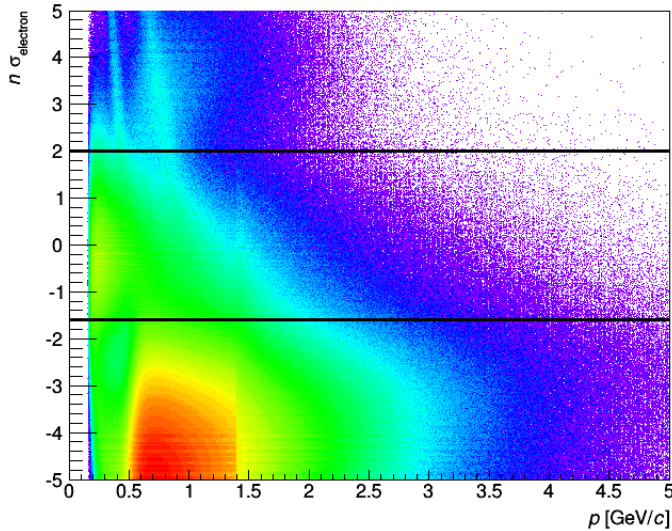


Figure 3.4: $n\sigma_{\mathrm{e}}$ of electron candidates satisfying TOF and BEMC cuts. Black lines denote the $n\sigma_{\mathrm{e}}$ cut.

24

### 3.3.2 TOF cut

As can be seen in the Figure 2.5 areas of specific energy loss of electrons, pions and protons overlap towards intermediate momenta, so it is needed to apply the TOF detector to distinguish different particle species in this region. For low momenta particles $1/\beta$ measured by TOF is $\sim 1$ for electrons while it is $> 1$ for heavier particles. Towards higher momenta ($p > 1.4$ GeV/$c$) $1/\beta$ of $e, \pi, p, K, d$ approaches to 1 and, therefore, it is not possible to distinguish between different particle species using only the TOF detector. So, the TOF cut is used only for particles with momenta lower than 1.4 GeV/$c$.

In our analysis the TOF cut was applied as follows: if $p < 1.4$ GeV/$c$ we required electron candidates to have a valid TOF signal, i.e. we required $|y_{\text{local}}| < 1.8$ cm where $y_{\text{local}}$ is distance of the track projection and the center of TOF pad and $1/\beta$ to be in the range from 0.97 to 1.025. This range was chosen as in previous analysis of $J/\psi$ in U+U collisions [42].

For particles with momenta higher than 1.4 GeV/$c$ TOF was used as veto − particle was accepted if it did not have the signal in TOF, however, if particle had the signal in TOF but $1/\beta$ was not in the required range it was not accepted.

Figure 3.5 shows $1/\beta$ of electron candidates with $p_{\text{T}} > 0.2$ GeV/$c$ which satisfy TPC and BEMC cut. The lines on the plot illustrate the TOF cut.
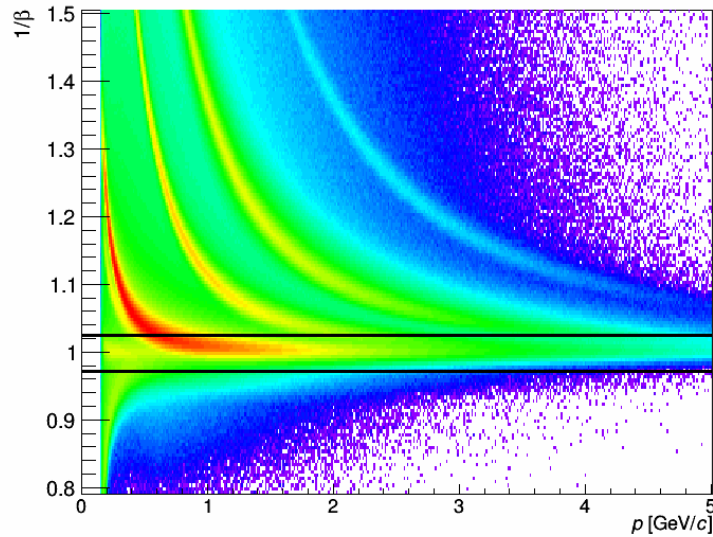


Figure 3.5: $1/\beta$ of particles which satisfy TPC and BEMC cuts. Black lines on the plot illustrate the TOF cut.

### 3.3.3 BEMC cut

To distinguish particles of momenta higher than 1.4GeV/$c$ the BEMC cut is needed. BEMC can distinguish between electrons and hadrons with higher momenta according to the ratio $pc/E$ ($E$ is deposited energy in the BEMC tower) which should be $\sim 1$ for electrons and $< 1$

for hadrons. However, different effects (leakage/gain of the energy to/from neighboring towers) modify this ratio. Electron candidates were required to deposit energy $E > 0.15\text{GeV}$ in the highest energy BEMC tower and satisfy the criterion: $0.7 < pc/E < 2.0$.

## 3.4 Raw $J/\psi$ yield

$J/\psi$ invariant mass was reconstructed from the decay of $J/\psi$ mesons into $e^-e^+$ pairs. To find the $J/\psi$ signal we combined each electron candidate with each positron candidate satisfying electron cuts described in previous section. The invariant mass was calculated according to the formula

$$m_{\text{inv}} = \sqrt{2\ p_1\ p_2\ (1 - \cos\ \alpha)} \tag{3.2}$$

where $p_1$ and $p_2$ are momenta of electron and positron candidates and $\alpha$ is the angle between $p_1$ and $p_2$. We used cut on $J/\psi$ rapidity: $-1 < y < 1$ to analyze signal only at midrapidity.

The way how we reconstructed $J/\psi$ signal includes combinatorial background which was needed to be subtracted. We used two methods of combinatorial background subtraction:

- **Like-sign background** - we combined electrons with electrons and positrons with positrons within the same events and reconstructed invariant mass of these pairs.

- **Mixed event background** - we combined electrons and positrons from different events with similar event conditions which were multiplicity and primary vertex position. For each multiplicity and $v_Z$ bin we calculated the combinatorial background combining each $e^+$ with each $e^-$ once at least 10 electron and positron candidates were obtained. Mixed event background was then normalized to the like-sign background in the invariant mass region (2.0, 4.2) $\text{GeV}/c^2$ around $J/\psi$ invariant mass. This method of combinatorial background subtraction enables us to increase the statistics (decrease the statistical error) compared with like-sign background.

Figure 3.6 shows the invariant mass spectra for the electron-positron unlike-sign pairs, mixed events pairs and like-sign pairs in 0-5% most central U+U collisions using different $p_T$ cuts on electron candidates. As can be seen, there is a small peak in the region around $J/\psi$ invariant mass $\sim 3.096\ \text{GeV}/c^2$ [26]. This peak is more visible towards higher $p_T$ cuts used on electron candidates, however, in these cases we have to deal with lower statistics. The $e^+e^-$ invariant mass spectra for the $p_T$ cuts $p_{T\ \text{electron}} > 0.2$ and $0.6\ \text{GeV}/c$ show almost no evidence of $J/\psi$ signal. Therefore, we do not use corresponding datasets in further analysis. We also show the $e^+e^-$ invariant mass spectrum for the $p_T$ cut $p_{T\ \text{electron}} > 1.4\ \text{GeV}/c$, however, since the peak of the di-electron invariant mass spectrum sits near $J/\psi$ invariant mass peak, we do not consider this option of the $p_{T\ \text{electron}}$ cut.

Due to its advantages we used the mixed event background for the description of the combinatorial background in further analysis. After the subtraction of the combinatorial background we still observed the residual background. This was fitted in the invariant mass region (2.0, 3.6) $\text{GeV}/c^2$. We used linear fit and polynomial fit of the second and third degree. The best result was obtained using the linear function for residual background fitting.
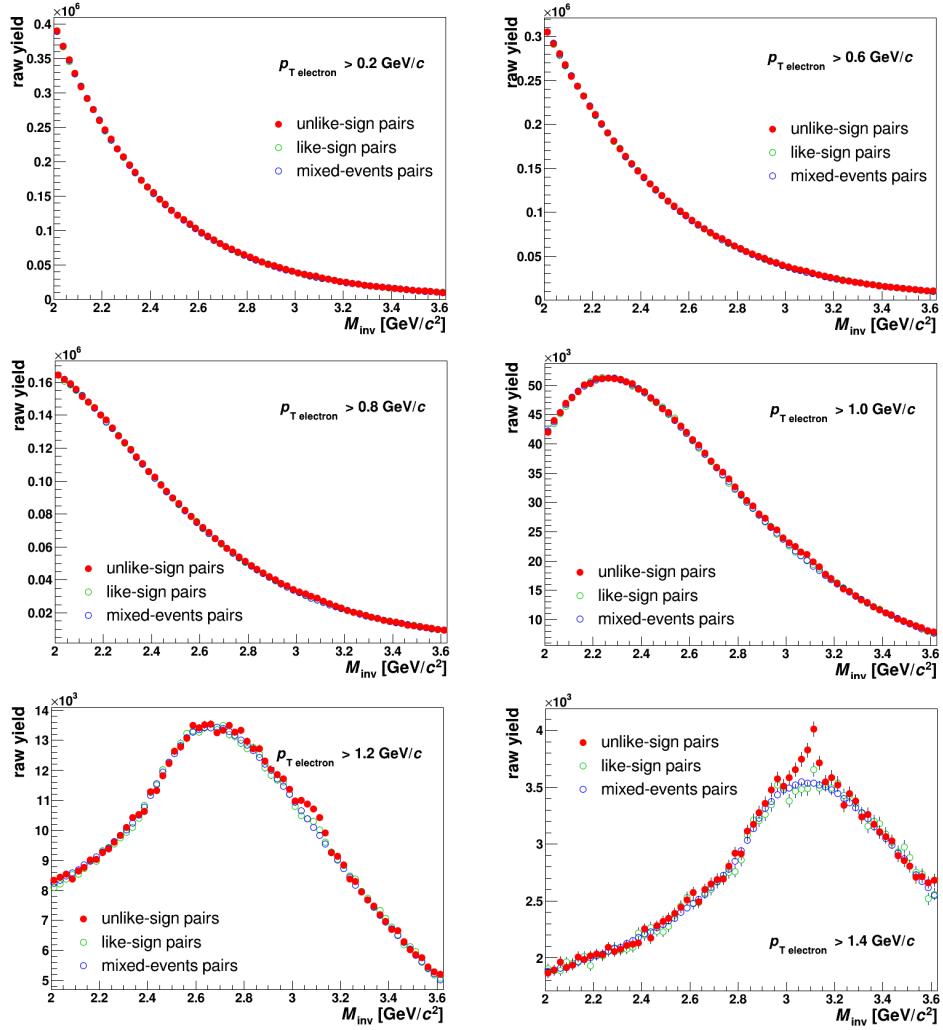
Figure 3.6: The invariant mass spectra of $e^+e^-$ unlike-sign pairs, mixed events pairs and like-sign pairs in 0-5% most central U+U collisions using different $p_T$ cuts on electron candidates.

Then, the invariant mass peak was fitted with Crystal ball function in the same region as the residual background. The Crystal ball function is similar to a Gaussian function with the power-low tail and can be expressed as [43]:

$$
f_{CB}(m) = \begin{cases} \frac{N}{\sqrt{2\pi}\sigma} \exp\left(-\frac{(m-m_0)^2}{2\sigma^2}\right), & \text{for } \frac{m-m_0}{\sigma} > -\alpha; \\ \frac{N}{\sqrt{2\pi}\sigma} \left(\frac{n}{|\alpha|}\right)^n \exp\left(-\frac{|\alpha|^2}{2}\right) \left(\frac{n}{|\alpha|} - |\alpha| - \frac{m-m_0}{\sigma}\right)^{-n}, & \text{for } \frac{m-m_0}{\sigma} \leq -\alpha. \end{cases}
\tag{3.3}
$$

$N$ is the normalization constant, $m_0$ is common mean (in our case $J/\psi$ invariant mass), $\sigma$ is variance, $\alpha$ defines the transition between the Gaussian and the power-law functions and $n$ describes an exponent of the power law tail [43].

In our fitting procedure we fixed the parameter $n$ at the same value as in previous analysis [42] and other parameters were left free. Figure 3.7 shows the invariant mass fits in 0-5% most central U+U collisions using different cuts on $p_{\text{T electron}}$ of electron candidates.

Raw $J/\psi$ yield was obtained by the bin counting in the invariant mass region (2.9-3.2) GeV/$c^2$ after subtracting the residual background. This range was motivated by the smearing of the yield towards lower invariant and the value of the variance. Significance $s$ of the $J/\psi$ signal can be calculated as

$$
s = \frac{S}{\sqrt{S+B}} = \frac{S}{\delta S}
\tag{3.4}
$$

where $S$ is the number of $J/\psi$ in chosen invariant mass region and $B$ is the background (combinatorial+residual) in the same region.

Table 3.1 shows an overview of data calculated using different $p_{\text{T}}$ cuts on electron candidates (denoted as "all" which means all $J/\psi$ $p_{\text{T}}$ included): raw yield and its error (calculated as error of bin counting combined with integral error of residual background) and significance. The highest significance was obtained for cut $p_{\text{T electron}} > 1.0$ GeV/$c$.

### 3.4.1 Raw $J/\psi$ yield in different $p_{\text{T}}$ bins

For three $p_{\text{T}}$ cuts on electron candidates ($p_{\text{T electron}} > 0.8, 1.0, 1.2$ GeV/$c$) we show invariant mass of the $J/\psi$ decay electron candidates in three $p_{\text{T}}$ bins: (0-1),(1-3) and (3-7) GeV/$c$ using the same methods as for $p_{\text{T}}$ integrated. The width of our $p_{\text{T}}$ bins was chosen due to small statistics. Results can be seen in the Figure 3.8 and summarized in the Table 3.1.

Here, the highest significance in the first and third $J/\psi$ $p_{\text{T}}$ bin and for $J/\psi p_{\text{T}}$ integrated were reasons why we favored and used the cut on electron candidates $p_{\text{T electron}} > 1.0$GeV/$c$ in further analysis described in following chapter.

However, at least, the tail of the Crystal Ball fit (see the Figures 3.7 and 3.8) is disputable − it can be seen in the Figure 3.8 that the width and the tail of the Crystal Ball peak is smallest in the highest $J/\psi p_{\text{T}}$ bin where we observe the least significant signal and this description of data does not seem to be physically reasonable. These two observations suggest that it is inappropriate to be satisfied only with these fits. Hence, for comparison we show Gaussian fitting of the $J/\psi$ signal in Appendix A. However, Gaussian fitting does not describe observed smearing of the peak for $m_{\text{inv}} < 3.1$GeV/$c^2$.
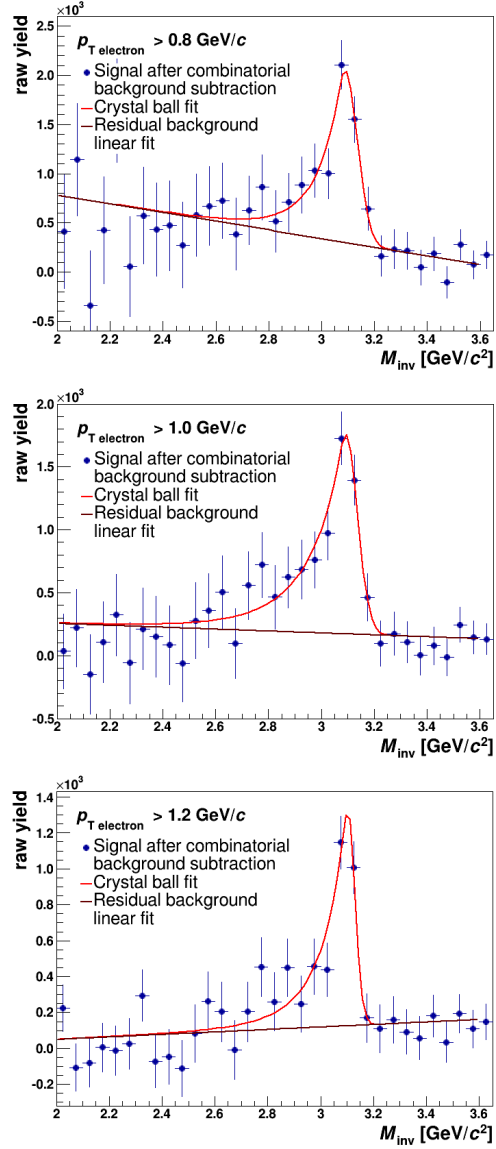
Figure 3.7: $J/\psi$ signal after combinatorial background subtraction for different cuts on $p_T$ of decay electron candidates. Signal is fitted with the Crystal Ball function, residual background with the linear function.
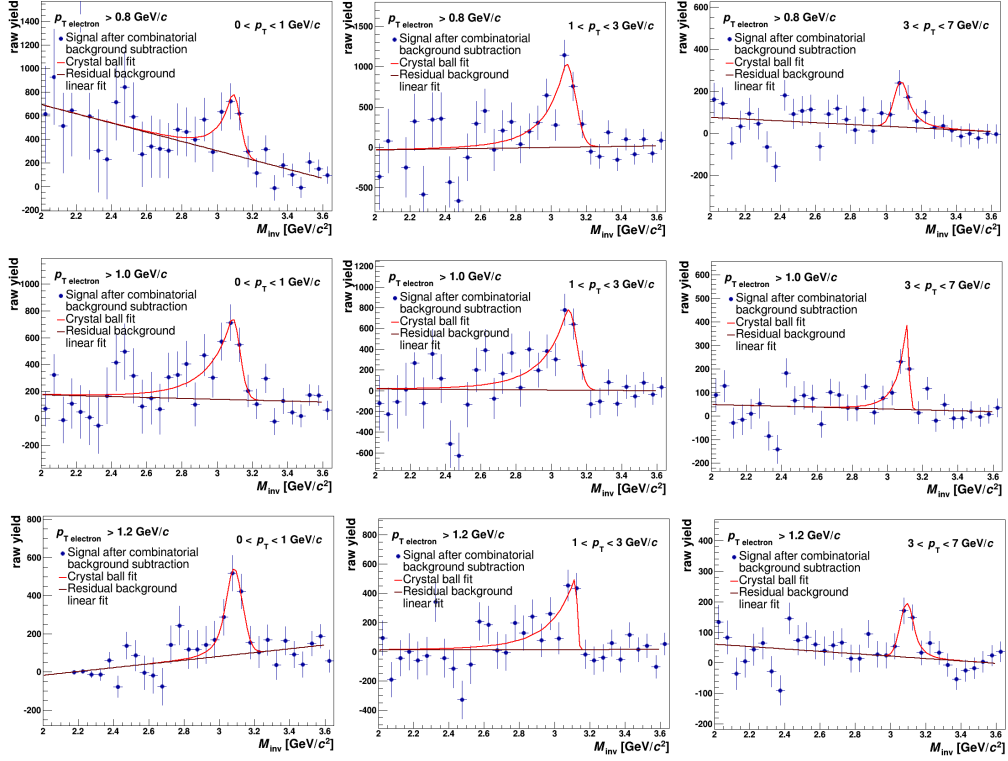
Figure 3.8: $J/\psi$ signal after combinatorial background subtraction for different cuts on $p_T$ of decay electron candidates and in different $J/\psi$ $p_T$ bins. Signal is fitted with the Crystal Ball function, residual background with the linear function.

| $p_T$ [GeV/$c$] | $p_{T\ electron} > 0.8$ GeV/$c$ | | |
|---|---|---|---|
| | Raw yield | Error | Significance |
| 0-1 | 1440 | 440 | 3.2 |
| 1-3 | 3420 | 520 | 6.6 |
| 3-7 | 490 | 160 | 3.0 |
| all | 5320 | 700 | 7.6 |
| $p_T$ [GeV/$c$] | $p_{T\ electron} > 1.0$ GeV/$c$ | | |
| | Raw yield | Error | Significance |
| 0-1 | 1980 | 370 | 5.3 |
| 1-3 | 2520 | 420 | 6.0 |
| 3-7 | 470 | 140 | 3.3 |
| all | 4960 | 580 | 8.6 |
| $p_T$ [GeV/$c$] | $p_{T\ electron} > 1.2$ GeV/$c$ | | |
| | Raw yield | Error | Significance |
| 0-1 | 1180 | 250 | 4.7 |
| 1-3 | 1220 | 290 | 4.2 |
| 3-7 | 340 | 110 | 3.1 |
| all | 2730 | 400 | 6.8 |

Table 3.1: Raw yield, error of the raw yield and significance in different $p_T$ bins of the $J/\psi$ signal of different $p_{T\ electron}$ cuts on decay electron candidates.

# Chapter 4

# Analysis of $J/\psi$ in central U+U collisions - signal corrections

$J/\psi$ raw yield presented in previous chapter is not the real number of $J/\psi$ produced in U+U collisions at midrapidity. There are some phenomena which cause a difference between the number of $J/\psi$ decayed via the di-electron decay channel and the number of $J/\psi$ calculated by the bin counting. These phenomena, quantified by $J/\psi$ reconstruction efficiency, cover efficiency of $J/\psi$ decay electron identification, TPC geometrical and tracking efficiency, signal counting correction, etc. In this chapter we deal in more detail with single electron identification efficiency.

## 4.1 Electron identification efficiency

The efficiency of electron identification covers cut efficiency − using different cuts on TPC, TOF and BEMC signal we analyzed only fraction of electrons accepted by the detector − and matching efficiency − which compares the number of electrons registered in a given detector with the number of all of them. Resulting efficiency of electron identification $\epsilon_e$ includes all mentioned efficiencies and can be expressed by the formula:

$$
\epsilon_e = \begin{cases}
\epsilon_{\text{TPCcut}} \times \epsilon_{\text{TOFcut}} \times \epsilon_{\text{TOFmatch}} & \text{for } p < 1.4 \text{GeV}/c; \\
\\
\epsilon_{\text{TPCcut}} \times [\epsilon_{\text{TOFcut}} \times \epsilon_{\text{TOFmatch}} + (1 - \epsilon_{\text{TOFmatch}})] \times \epsilon_{\text{BEMCcut}} \times \epsilon_{\text{BEMCmatch}} & \\
& \text{for } p > 1.4 \text{GeV}/c.
\end{cases}
\tag{4.1}
$$

As can be seen, there are two formulas how $\epsilon_e$ can be calculated since there are different requirements which tracks have to fulfill to be considered as electrons depending on the momenta of the tracks and the fact if the TOF or BEMC detector is used for particle identification.

In order to calculate different components of electron identification efficiency from data (described in following sections) we need to select pure electron data sample (in an ideal case) without hadron contamination. For this purpose we selected pairs of photonic electrons

(mostly from $\gamma$ conversions, $\pi^0$ and $\eta$ decays) with invariant mass $m_{\mathrm{inv}} < 10$ MeV/$c^2$ and with transverse momenta $p_{\mathrm{T}} > 1.0$ GeV/$c$ (as required for $J/\psi$ decay electron candidates).

To improve purity of our data sample we applied all detector cuts on one photonic electron candidate from the pair and saved the other one which was not biased by the studied detector. However, this purity improvement results in low statistics of our data sample.

## 4.2 TPC cut efficiency

Here we had to select photonic electron candidates using only TOF and BEMC cuts, however due to the method we used for saving electron candidates, this was provided only in a small range of $n\sigma_{\mathrm{e}}$: $-1.8 < n\sigma_{\mathrm{e}} < 2.5$. Therefore, we used the following method of TPC cut efficiency extraction(which can be seen in the Figure 4.1): in each momentum bin we fitted the
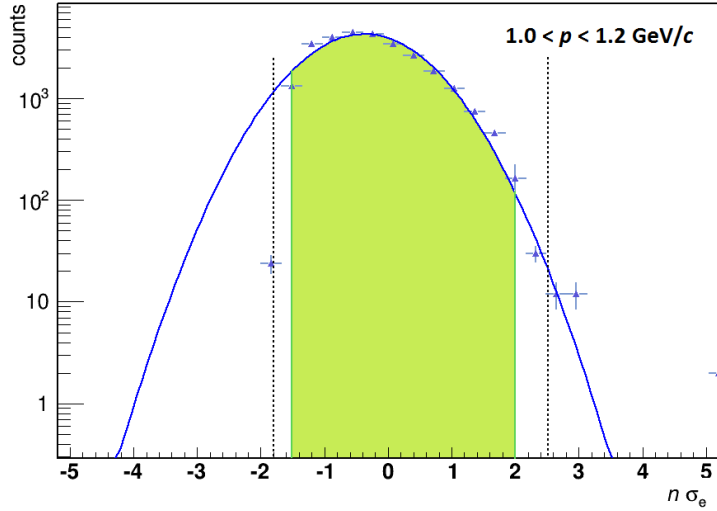


Figure 4.1: $n\sigma_{\mathrm{e}}$ of photonic electron candidates in one momentum bin: $1.0 < p < 1.2$ GeV/$c$.

$n\sigma_{\mathrm{e}}$ distribution with Gaussian function (blue curve) in the given range (black dotted lines) and then compared the area under the part of the Gaussian curve in the range $-1.5 < n\sigma_{\mathrm{e}} < 2.0$ (this range is given by our TPC cut on $J/\psi$ decay electron candidates, shown as green area) with the area under the Gaussian curve in its whole range.

The purity of our data sample was improved by subtracting the like-sign background of photonic electrons, i.e. positron-positron and electron-electron pairs with invariant mass of the pair $m_{\mathrm{inv}} < 10$ MeV/$c^2$, from the unlike-sign data sample.

Resulting TPC cut efficiency given as a function of photonic electron momentum can be seen in the the Figure 4.2. It shows unexpected non-constant trend and significant increase of the statistical error towards higher momenta probably caused by the significant decrease of photonic electron candidates. Therefore, our aim is to improve the method for saving the electron candidates and thus increase the statistics needed for TPC cut efficiency calculation.
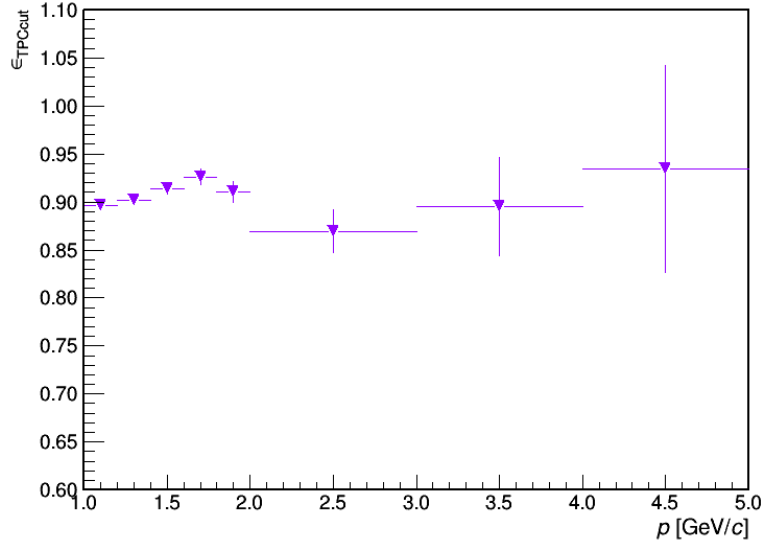
Figure 4.2: TPC cut efficiency given as a function of photonic electron momentum.

## 4.3 TOF efficiency

In order calculate the TOF cut and TOF matching efficiency we selected photonic electron candidates using the TPC and BEMC cuts only.

### 4.3.1 TOF cut efficiency

From electron candidates we required $0.97 < 1/\beta < 1.025$. The TOF cut efficiency was calculated as the ratio of the number of photonic electron candidates satisfying mentioned $1/\beta$ cut to the number of photonic electron candidates satisfying following wider cut: $0.93 < 1/\beta < 1.07$. Figure 4.3 shows $1/\beta$ of photonic electron candidates in one momentum bin ($1.2 < p < 1.4$ GeV/$c$), blue area denotes the electron candidates satisfying narrower $1/\beta$ cut while blue lines denote the wider $1/\beta$ range.

Since required TOF cut was chosen wide enough to cover most of the electron candidates, resulting TOF cut efficiency is $\sim 1$. Figure 4.4 shows the TOF cut efficiency as a function of particle momentum.

35
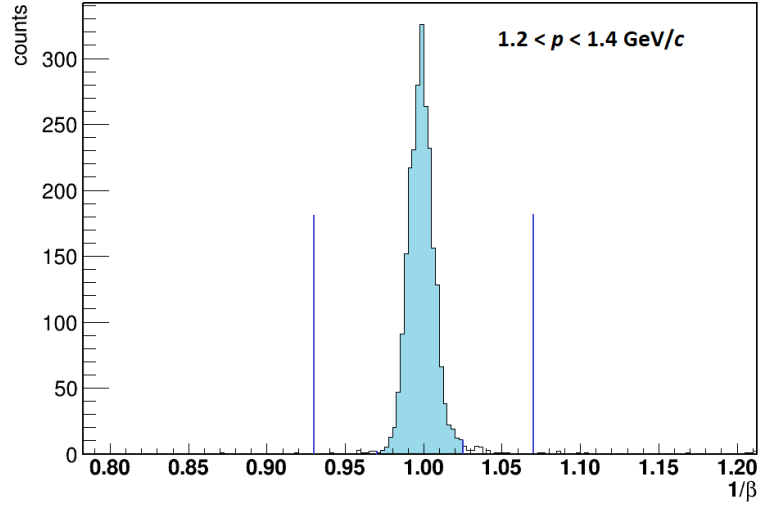
Figure 4.3: $1/\beta$ of photonic electron candidates in one momentum bin: $1.2 < p < 1.4$ GeV/$c$.
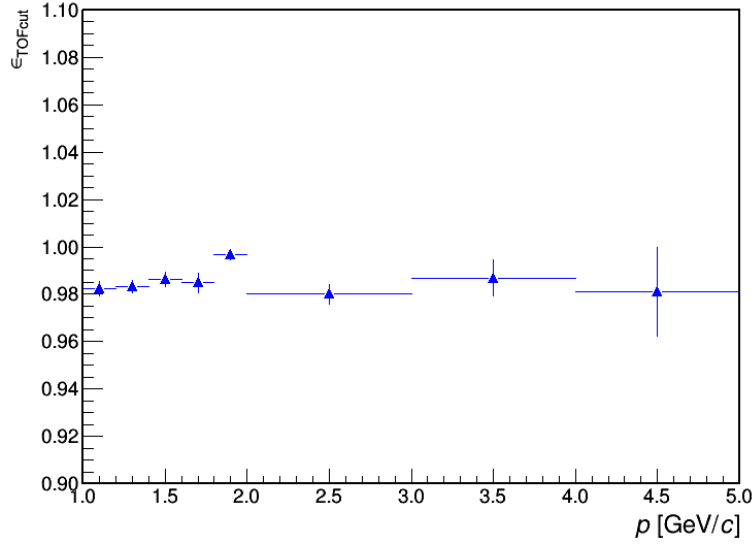


Figure 4.4: TOF cut efficiency as a function of photonic electron momentum.

### 4.3.2 TOF matching efficiency

TOF matching efficiency was calculated as the ratio of the number of photonic electron candidates with valid TOF signal and all photonic electron candidates.

The Figure 4.5 shows resulting TOF matching efficiency as a function of photonic electron momentum.
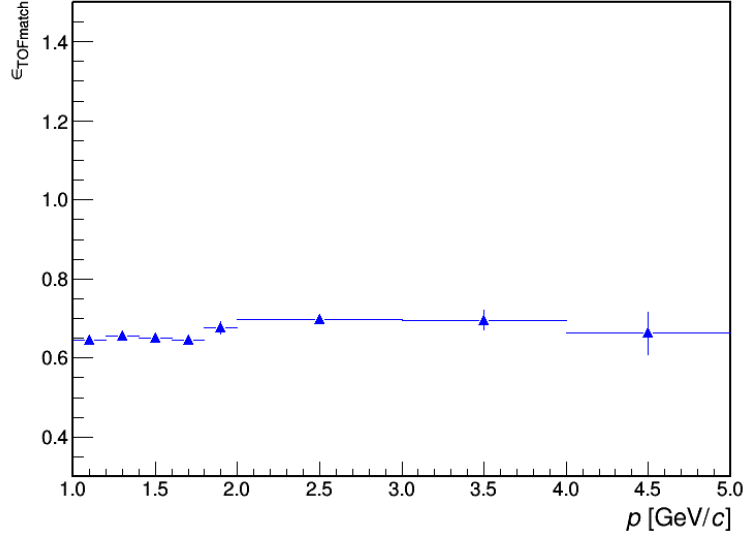
Figure 4.5: TOF matching efficiency as a function of photonic electron momentum.

## 4.4 BEMC efficiency

### 4.4.1 BEMC cut efficiency

For the BEMC cut efficiency calculation we selected photonic electron candidates using the TPC and TOF cut only. The BEMC cut efficiency is calculated as the ratio of photonic electrons which satisfy the requirement $0.7 < pc/E < 2.0$ to all of them. To improve the purity of our data sample, like-sign background of photonic electrons was subtracted from our unlike-sign data sample.

Figure 4.6 shows $p/E$ ($c = 1$) of photonic electron candidates in one momentum bin ($1.4 < p < 1.6$ GeV/$c$). Filled area shows the BEMC cut. Unlike-sign photonic electron candidates, like-sign background and subtracted data sample used for further calculation of the BEMC cut efficiency are shown in different colors (red, blue, purple).

Figure 4.7 shows resulting BEMC cut efficiency as a function of electron momentum.

### 4.4.2 BEMC matching efficiency

In order calculate the BEMC matching efficiency we selected photonic electron candidates using TPC cut only since there is a correlation between the probability that electron will have a signal in TOF and a probability that it will have a signal in BEMC. The resulting BEMC efficiency is than calculated as the ratio of the number of photonic electron candidates with valid BEMC signal and all photonic electron candidates.

Figure 4.8 shows resulting BEMC matching efficiency as a function of photonic electron momentum.
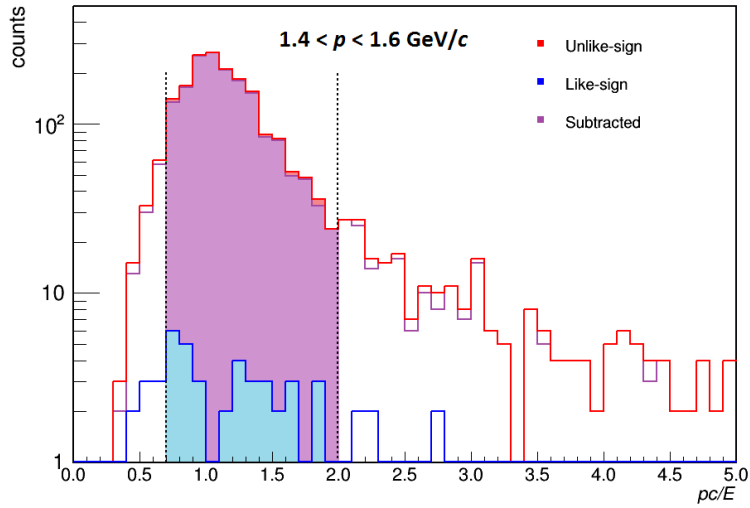
Figure 4.6: $p/E$ of photonic electron candidates in one momentum bin, $1.4 < p < 1.6$ GeV/$c$.
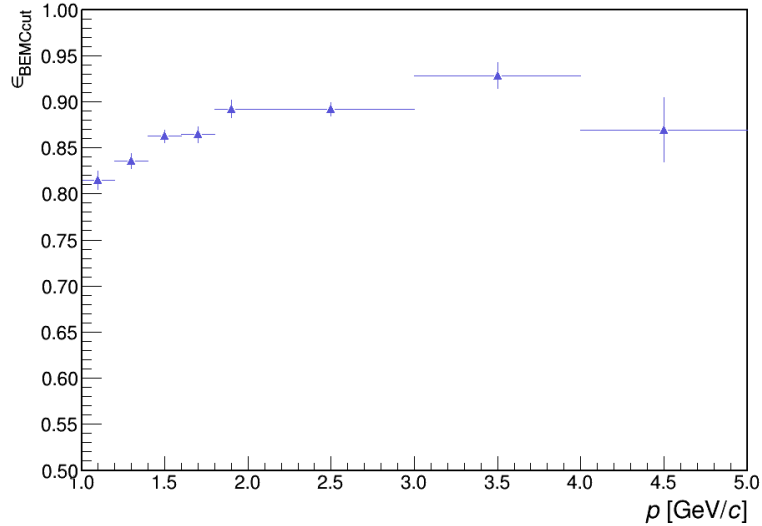


Figure 4.7: BEMC cut efficiency as a function of electron momentum.

### 4.4.3   Single electron identification efficiency

Figure 4.9 shows the resulting single electron identification efficiency as a function of particle momentum calculated using 4.1. Efficiency shows discontinuity around $p = 1.4$ GeV/$c$ which is caused mainly by the change in the requirements on electron candidates. However, due to the low statistics this result is approximate only and will be improved using larger data sample.
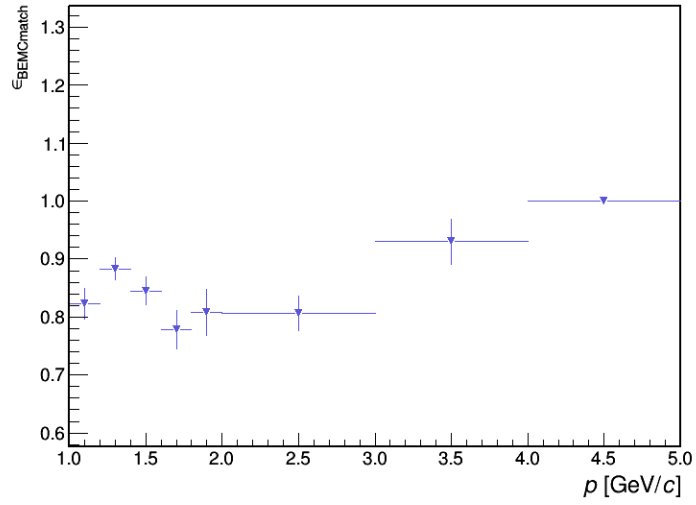
Figure 4.8: BEMC matching efficiency as a function of photonic electron momentum.
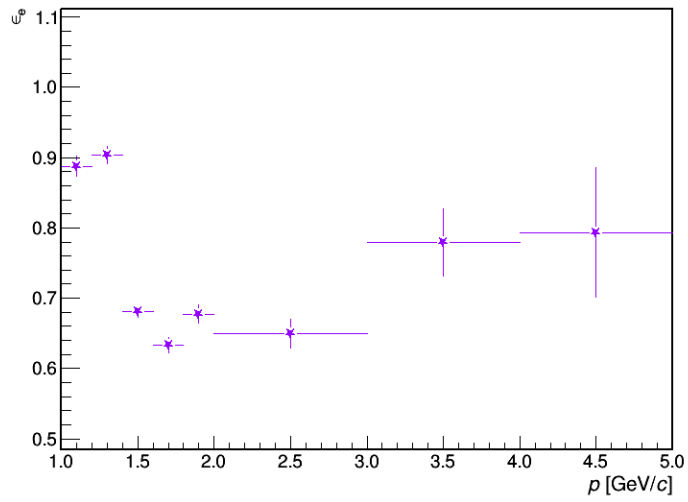


Figure 4.9: Resulting single electron identification efficiency as a function of particle momentum.

# Conclusions and Outlook

The aim of this research project was to present results on $J/\psi$ production measurements via the decay channel $J/\psi \rightarrow e^{-}e^{+}$ in centrally triggered 0-5% most central U+U collisions at the center-of-mass energy $\sqrt{s_{\mathrm{NN}}} = 193$ GeV at the STAR experiment. In this colliding system the effects of the hot medium are expected to be most significant over the whole centrality range and among all nuclei which have been colliding at RHIC until now. The study of $J/\psi$ production in such colliding system is, therefore, challenging.

We briefly presented theoretical motivation for our studies and described the STAR detector and its subsystems. Information obtained by three of them, TPC, TOF and BEMC, was used to electron (positron) identification followed by extraction of $J/\psi$ raw yield. We observe $J/\psi$ signal of significance $\sim 8.6$ $\sigma$ for $p_{\mathrm{T}}$ integrated. Dividing into different $p_{\mathrm{T}}$ bins the significance of $J/\psi$ signal decreases towards higher $p_{\mathrm{T}}$.

We also described our method of single electron identification efficiency extraction and demonstrated this method on photonic electron data sample. This is the first step in the overall $J/\psi$ reconstruction efficiency calculation.

Next aim of our analysis is the extraction of $J/\psi$ invariant yield and nuclear modification factor in 0-5% most central U+U collisions. To perform this task, we plan to finish our signal corrections. We will include results of simulations and calculate systematic uncertainties.

It will be also very important to provide centrality correction of our data since centrally triggered U+U collisions are selected using TOF and ZDC triggers which set low threshold for interpreting collisions as 0-5% most central.

As already mentioned, results of our analysis will serve an information about centrality behavior of $J/\psi$ production in U+U collisions. It will be also interesting to compare our results with results in 0-5% most central Au+Au collisions. Although the nuclear modification factor in minimum bias U+U collisions is similar to that in Au+Au collisions, the results in the most central region can be significantly different.

# Bibliography

[1] J. C. Collins and M. J. Perry. Superdense Matter: Neutrons or Asymptotically Free Quarks ? *Phys. Rev. Lett.*, 34:1353–1356, May 1975.

[2] B. V. Jacak and B. Müller. The Exploration of Hot Nuclear Matter. *Science*, 337:310–314, July 2012.

[3] M. Harrison, T. Ludlam, and S. Ozaki. Rhic project overview. *Nuclear Instruments and Methods in Physics Research Section A: Accelerators, Spectrometers, Detectors and Associated Equipment*, 499(2–3):235–244, 2003. The Relativistic Heavy Ion Collider Project: RHIC and its Detectors.

[4] Wolfram Fischer. Run overview ofthe Relativistic Heavy Ion Collider. `http://www.rhichome.bnl.gov/RHIC/Runs/`. [online 10.06.2015].

[5] BNL. The Relativistic Heavy Ion Collider Run-14. `http://www.rhichome.bnl.gov/AP/RHIC2014/`. [online 10.06.2015].

[6] H. Satz S. Sarkar and B. Sinha. *The Physics of the Quark-Gluon Plasma A: Introductory Lectures.* Springer, Berlin Heidelberg, 1st edition, 2010.

[7] Michael Kliemant, Raghunath Sahoo, Tim Schuster, and Reinhard Stock. Global properties of nucleus–nucleus collisions. In Sourav Sarkar, Helmut Satz, and Bikash Sinha, editors, *The Physics of the Quark-Gluon Plasma*, volume 785 of *Lecture Notes in Physics*, pages 23–103. Springer Berlin Heidelberg, 2010.

[8] Daniel Kikola, Grazyna Odyniec, and Ramona Vogt. Prospects for quarkonia production studies in u + u collisions. *Phys. Rev. C*, 84:054907, Nov 2011.

[9] P.P. Bhaduri, P. Hegde, H. Satz, and P. Tribedy. An introduction to the spectral analysis of the qgp. In Sourav Sarkar, Helmut Satz, and Bikash Sinha, editors, *The Physics of the Quark-Gluon Plasma*, volume 785 of *Lecture Notes in Physics*, pages 179–197. Springer Berlin Heidelberg, 2010.

[10] T. Matsui and H. Satz. $J/\psi$ Suppression by Quark-Gluon Plasma Formation. *Phys.Lett.*, B178:416, 1986.

[11] Ramona Vogt. *Ultrarelativistic Heavy-Ion Collisions.* Elsevier, Amsterdam, 1st edition, 2007.

[12] Cheuk-Yin Wong. *Introduction to High-Energy Heavy Ion collisions.* Utopia Press, Singapore, 1st edition, 1994.

[13] A. Adare et al. Measurement of $\Upsilon$(1S+2S+3S) production in p+p and Au+Au collisions at $\sqrt{s_{NN}} = 200$ GeV. 2014.

[14] Taku Gunji. *J/$\psi$ Production in High Energy Heavy Ion Collisions at RHIC*. PhD thesis, University of Tokyo, 2007.

[15] Jean Paul Blaizot, Francois Gelis, and Raju Venugopalan. High-energy pA collisions in the color glass condensate approach. 1. Gluon production and the Cronin effect. *Nucl.Phys.*, A743:13–56, 2004.

[16] A. Krzywicki, J. Engels, B. Petersson, and U. Sukhatme. Does a nucleus act like a gluon filter? *Physics Letters B*, 85(4):407 – 412, 1979.

[17] M.J. Leitch. Quarkonia production at RHIC. *J.Phys.*, G32:S391–S400, 2006.

[18] Xingbo Zhao and Ralf Rapp. Charmonium in medium: From correlators to experiment. *Phys. Rev. C*, 82:064905, Dec 2010.

[19] S. Digal, P. Petreczky, and H. Satz. Quarkonium feed down and sequential suppression. *Phys.Rev.*, D64:094015, 2001.

[20] Yunpeng Liu, Zhen Qu, Nu Xu, and Pengfei Zhuang. transverse momentum distribution in high energy nuclear collisions. *Physics Letters B*, 678(1):72 – 76, 2009.

[21] L. Adamczyk et al. *J/$\psi$* production at high transverse momenta in p+p and Au+Au collisions at $\sqrt{s_{NN}} = 200$ GeV. *Phys.Lett.*, B722:55–62, 2013.

[22] Wangmei Zha. Recent measurements of quarkonium production in and a + a collisions from the star experiment. *Nuclear Physics A*, 931:596–600, 2014. Quark Matter 2014XXIV International Conference on Ultrarelativistic Nucleus-Nucleus Collisions.

[23] Brookhaven National Laboratory. RHIC Accelerators. `http://www.bnl.gov/rhic/complex.asp`. [online 29.03.2015].

[24] M. Anderson, J. Berkovitz, W. Betts, R. Bossingham, F. Bieser, et al. The Star time projection chamber: A Unique tool for studying high multiplicity events at RHIC. *Nucl.Instrum.Meth.*, A499:659–678, 2003.

[25] The STAR Collaboration. A Proposal for STAR Inner TPC Sector Upgrade (iTPC). June 2015.

[26] H. Bichsel, D.E. Groom, and S.R. Klein. Passage of particles through matter. `http://pdg.lbl.gov/2006/reviews/passagerpp.pdf`. [online 05.04.2015].

[27] M. Shao, O. Barannikova, X. Dong, Y. Fisyak, L. Ruan, et al. Extensive particle identification with TPC and TOF at the STAR experiment. *Nucl.Instrum.Meth.*, A558:419–429, 2006.

[28] T.M. Cormier, A.I. Pavlinov, M.V. Rykov, V.L. Rykov, and K.E. Shestermanov. STAR barrel electromagnetic calorimeter absolute calibration using 'minimum ionizing particles' from collisions at RHIC. *Nucl.Instrum.Meth.*, A483:734–746, 2002.

[29] STAR Collaboration. SketchUp STAR. `https://drupal.star.bnl.gov/STAR/subsys/bemc`. [online 20.06.2015].

[30] K. Schweda. A Heavy-flavor tracker for STAR. *Nucl.Phys.*, A774:907–910, 2006.

[31] Rongrong Ma, Hao Qiu. Hard Probe Highlights. STAR Collaboraton Meetng, Stony Brook, June 2015.

[32] STAR Collaboration. MTD plots, pictures and photos. `https://drupal.star.bnl.gov/STAR/subsys/mtd/plots-pictures`. [online 29.06.2015].

[33] C. Yang, X.J. Huang, C.M. Du, B.C. Huang, Z. Ahammed, et al. Calibration and performance of the STAR Muon Telescope Detector using cosmic rays. 2014.

[34] L. Ruan, G. Lin, Z. Xu, K. Asselta, H.F. Chen, et al. Perspectives of a Midrapidity Dimuon Program at RHIC: A Novel and Compact Muon Telescope Detector. *J.Phys.*, G36:095001, 2009.

[35] Petr Chaloupka for The STAR Collaboration. Heavy quarkonium production at the STAR experiment. EPS Conference on High Energy Physics, July 2015.

[36] Tom Trainor and J.G. Reid. Level 2 Trigger Simulation Documents. `https://www.star.bnl.gov/public/trg/GeneralTrigger/Simulations/level_2/level_2.html`.

[37] James P. Whitfield. Level 0 Simulation Analysis, Introduction. `https://www.star.bnl.gov/public/trg/GeneralTrigger/Simulations/level_0/level0_intro.html`.

[38] W.J. Llope, J. Zhou, T. Nussbaum, G.W. Hoffmann, K. Asselta, et al. The STAR Vertex Position Detector. 2014.

[39] Christopher Beresford Powell. *J/ψ Production in Heavy Ion Collisions at the STAR Detector at RHIC.* PhD thesis, University of Cape Town, 2012.

[40] F.S. Bieser, H.J. Crawford, J. Engelage, G. Eppley, L.C. Greiner, E.G. Judd, S.R. Klein, F. Meissner, R. Minor, Z. Milosevich, G. Mutchler, J.M. Nelson, J. Schambach, A.S. VanderMolen, H. Ward, and P. Yepes. The STAR trigger. *Nuclear Instruments and Methods in Physics Research Section A: Accelerators, Spectrometers, Detectors and Associated Equipment*, 499(2-3):766–777, 2003. The Relativistic Heavy Ion Collider Project: RHIC and its Detectors.

[41] Chi Yang, for the STAR Collaboration. Performance of the Muon Telescope Detector (MTD) in STAR at RHIC. Quark Matter 2012.

[42] Ota Kukral for the STAR Collaboration. J/ψ production in $U + U$ collisions at $\sqrt{s_{NN}} = 193$ GeVin the STAR experiment. Proceedings of Science. The European Physical Society Conference on High Energy Physics -EPS-HEP2013.

[43] Serguei Chatrchyan et al. Suppression of non-prompt $J/\psi$, prompt $J/\psi$, and Y(1S) in PbPb collisions at $\sqrt{s_{NN}} = 2.76$ TeV. *JHEP*, 05:063, 2012.

# Appendix A

# Fitting of $J/\psi$ signal with Gaussian function

    Figure A.1 shows Gaussian fitting of $J/\psi$ invariant mass for $J/\psi$ $p_T$ integrated. Three blocks of the figure represent three different $p_T$ cuts applied on $J/\psi$ decay electron candidates. Figure A.2 shows Gaussian fitting of $J/\psi$ invariant mass for three $J/\psi$ $p_T$ bins, (0-1), (1-3) and (3-7) GeV/$c$ and for three different $p_T$ cuts applied on $J/\psi$ decay electron candidates. Table A.1 summarizes raw yield, its error and significance for each $J/\psi p_T$ bin and $p_{T\text{ electron}}$ cut using Gaussian fitting. In this case, the raw yield was calculated in the region $\sim$ $\pm$ 3 $\sigma$ around the mean value, i.e. (3.0, 3.2).

| $p_{\mathrm{T}}$ [GeV/$c$] | $p_{\mathrm{T\ electron}} > 0.8$ GeV/$c$ | | |
|:---:|:---:|:---:|:---:|
| | Raw yield | Error | Significance |
| 0-1 | 1390 | 400 | 3.4 |
| 1-3 | 3210 | 490 | 6.6 |
| 3-7 | 480 | 150 | 3.1 |
| all | 5050 | 650 | 7.7 |
| $p_{\mathrm{T}}$ [GeV/$c$] | $p_{\mathrm{T\ electron}} > 1.0$ GeV/$c$ | | |
| | Raw yield | Error | Significance |
| 0-1 | 1900 | 350 | 5.4 |
| 1-3 | 2400 | 400 | 6.0 |
| 3-7 | 460 | 130 | 3.5 |
| all | 4750 | 550 | 8.7 |
| $p_{\mathrm{T}}$ [GeV/$c$] | $p_{\mathrm{T\ electron}} > 1.2$ GeV/$c$ | | |
| | Raw yield | Error | Significance |
| 0-1 | 1160 | 240 | 4.8 |
| 1-3 | 1150 | 260 | 4.2 |
| 3-7 | 340 | 110 | 3.1 |
| all | 2640 | 380 | 6.9 |

Table A.1: Raw yield, error of the raw yield in different $J/\psi$ $p_{\mathrm{T}}$ bins and significance of the $J/\psi$ signal of different $p_{\mathrm{T}}$ cuts on decay electron candidates.
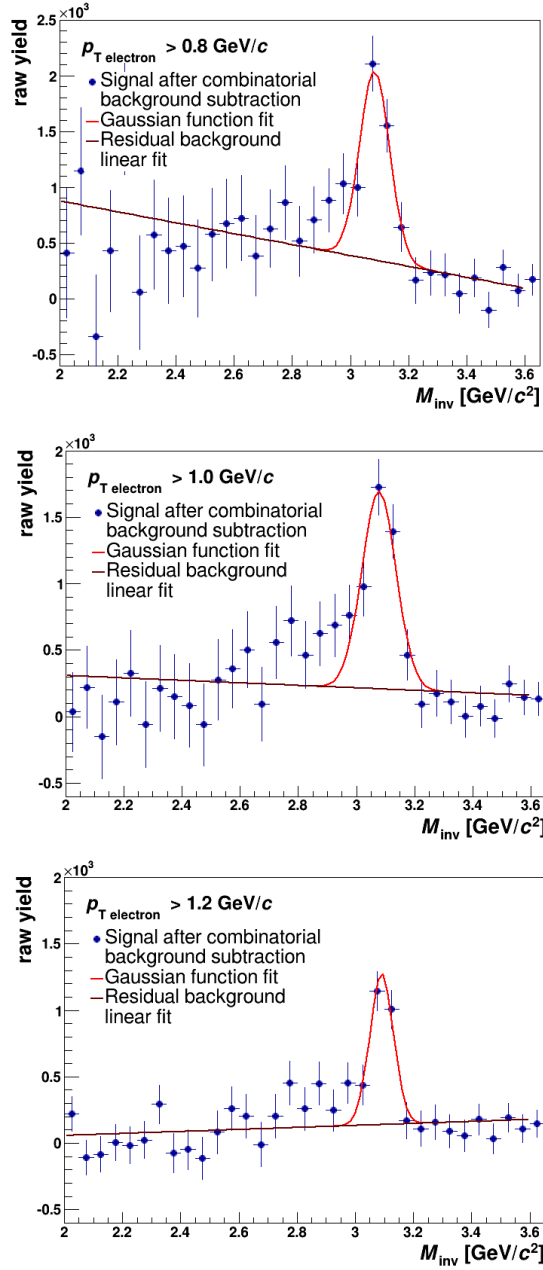
Figure A.1: $J/\psi$ invariant mass for $J/\psi$ $p_T$ integrated. Three blocks of the figure represent three different $p_T$ cuts applied on $J/\psi$ decay electron candidates.
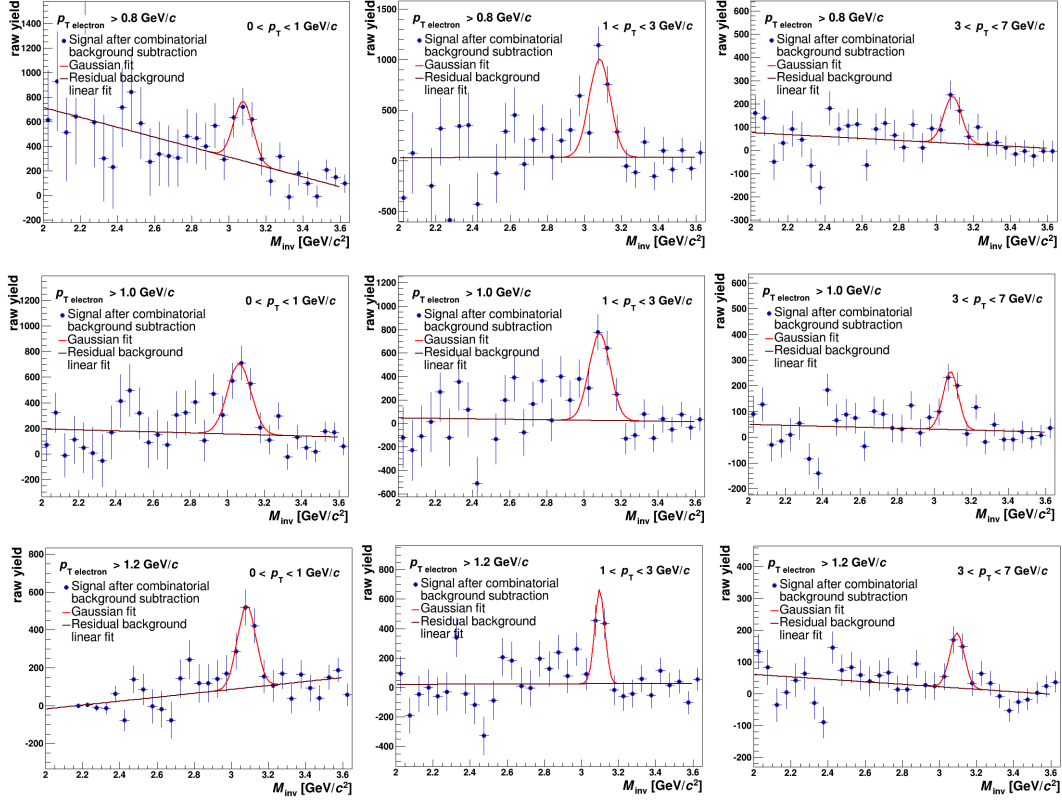
Figure A.2: Gaussian fitting of $J/\psi$ invariant mass for three $J/\psi$ $p_{\text{T}}$ bins, (0-1), (1-3) and (3-7) GeV/$c$ and for three different $p_{\text{T}}$ cuts applied on $J/\psi$ decay electron candidates.